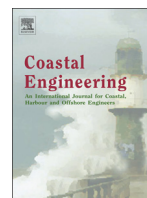




Contents lists available at ScienceDirect

Coastal Engineering

journal homepage: [www.elsevier.com/locate/coastaleng](http://www.elsevier.com/locate/coastaleng)

## The SPAIR method: Isolating incident and reflected directional wave spectra in multidirectional wave basins

S. Draycott<sup>a,\*</sup>, T. Davey<sup>a</sup>, D.M. Ingram<sup>b</sup>, A. Day<sup>c</sup>, L. Johanning<sup>d</sup>

<sup>a</sup> FloWave Ocean Energy Research Facility, Max Born Crescent, King's Buildings, Edinburgh EH9 3BF, UK

<sup>b</sup> Institute for Energy Systems, School of Engineering, The University of Edinburgh, Edinburgh EH9 3JL, UK

<sup>c</sup> Naval Architecture and Marine Engineering, The University of Strathclyde, Glasgow G4 0LZ, UK

<sup>d</sup> Renewable Energy Research Group, University of Exeter, TR10 9E, UK

### ARTICLE INFO

#### Article history:

Received 3 June 2015

Received in revised form 6 April 2016

Accepted 9 April 2016

Available online xxxx

#### Keywords:

SPAIR

Tank testing

Directional spectrum measurement

FloWave

Phase-Time-Path-Difference

Wave reflection

Single-summation method

### ABSTRACT

Wave tank tests aiming to reproduce realistic or site specific conditions will commonly involve using directionally spread, short-crested sea states. The measurement of these directional characteristics is required for the purposes of calibrating and validating the modelled sea state. Commonly used methods of directional spectrum reconstruction, based on directional spreading functions, have an inherent level of uncertainty associated with them. In this paper we aim to reduce the uncertainty in directional spectrum validation by introducing the SPAIR (Single-summation PTPD Approach with In-line Reflections) method, in combination with a directional wave gauge array. A variety of wave conditions were generated in the FloWave Ocean Energy Research Facility, Edinburgh, UK, to obtain a range of sea state and reflection scenarios. The presented approach is found to provide improved estimates of directional spectra over standard methods, reducing the mean apparent directional deviation down to below 6% over the range of sea states. Additionally, the method isolates incident and reflected spectra in both the frequency and time domain, and can separate these wave systems over 360°. The accuracy of the method is shown to be only slightly sensitive to the level of in-line reflection present, but at present cannot deal with oblique reflections. The SPAIR method, as presented or with slight modification, will allow complex directional sea states to be validated more effectively, enabling multidirectional wave basins to simulate realistic wave scenarios with increased confidence.

© 2016 The Authors. Published by Elsevier B.V. This is an open access article under the CC BY license (<http://creativecommons.org/licenses/by/4.0/>).

### 1. Introduction

Wave tank tests facilitate the understanding of how complex sea conditions influence the dynamics of man-made structures. A key requirement for any test programme is the ability to create these conditions in a highly controlled and repeatable manner. To have such control, it is vital to be able to measure and validate the desired test conditions. Whilst this is a relatively simple task when generating uni-directional waves, the extension to the measurement and validation of directional spectra can be challenging.

The experimental measurements presented here were made at the FloWave Ocean Energy Research Facility, located at the University of Edinburgh (Fig. 1). The facility consists of a circular 25 m diameter, 2 m depth combined wave and current test basin which is encircled by 168 active-absorbing force-feedback wavemakers. This geometry and design are intended to remove any inherent limitation on wave direction and therefore allow the recreation of highly spread and highly complex

directional spectra. As such, it presents an ideal environment to explore and demonstrate directional measurement methodologies.

To validate a directional spectrum, a method of reconstruction is required. Most of these methods aim to resolve the frequency-dependent Directional Spreading Function (DSF), thus describing the distribution of wave energy with direction. These methods use the measured cross-spectra between wave gauges, along with the known gauge positions, to fit a directional distribution. There are a number of approaches in doing this, with some commonly used approaches being the Bayesian Directional Method (BDM) (Hashimoto and Konbune, 1988), the Maximum Likelihood Method (MLM) (Benoit et al., 1997; Krogstad, 1988), and the Extended Maximum Entropy Principal (EMEP) (Hashimoto et al., 1994).

The nature of DSF-based reconstruction methods means that there is some uncertainty associated with the estimate. In this work we use a combined wave generation-measurement approach that enables the directional spectra to be estimated with increased certainty, whilst additionally enabling the isolation of incident and reflected components under certain conditions. This method has been named SPAIR, or the Single-summation PTPD Approach with In-line Reflections, and enables directional sea states to be validated with greater confidence.

\* Corresponding author.

E-mail address: [S.Draycott@ed.ac.uk](mailto:S.Draycott@ed.ac.uk) (S. Draycott).



Fig. 1. The FloWave Ocean Energy Research Facility.

To generate the waves a single-summation method is used (Miles and Funke, 1989) ensuring that each discrete frequency component only has one propagation direction. This enables meaningful frequency dependent wave directions to be inferred from a wave gauge array, using a Phase-Time-Path-Difference (PTPD) approach (Esteva, 1976), providing an estimate of the directional spectrum. This approach is demonstrated by Draycott et al. (2015), and has been shown to be significantly more effective than both the EMEP and BDM methods at estimating directional spectra when combined with single-summation wave generation. In this paper the method is demonstrated over a larger test matrix, designed to explore the reconstruction effectiveness over a range of peak frequencies, directional spreading and peak steepness. Additional complex spectra are explored, which highlight the benefit of using this approach when analysing highly spread or multi-modal spectra.

The SPAIR method, as employed in FloWave, uses the PTPD approach and calculated directions to perform in-line reflection analysis using a least squares method, similar to Zelt and Skjelbreia (1992). Under the assumption that reflections mirror the incident, this enables the reflected directional spectrum to be isolated, with phase information, enabling both incident and reflected time-series to be reconstructed.

Limits of the method assumptions are explored, particularly relating how the magnitude and angle of reflections affect both the incident angle calculation, and on the separation of incident and reflected components. In addition, alternative uses of these single-summation based tools are discussed for different purposes, and for when the SPAIR method assumptions are inappropriate.

## 2. Methodology

### 2.1. Sea state input and generation

#### 2.1.1. Input sea states

To examine the SPAIR method performance under a range of representative conditions, 27 parametric sea states were created and tested at the facility. These tests cover a range of peak frequencies,  $f_p$ , directional spreading,  $s$ , and peak wave steepness,  $s_p$  (defined as  $H_{m0}/L_p$ , where  $H_{m0}$  is the significant wave height, and  $L_p$  is the peak wavelength). All of the sea states were created using JONSWAP spectra with a constant gamma value of 3.3. In addition to this, a range of mean directions were then considered, examining the influence of the wave gauge orientation on

Table 1  
Main 3 × 3 × 3 test matrix (27 tests in total).

Wave parameter	Range of values		
Peak frequency, $f_p$ [Hz]	0.45	0.6	0.75
cos-2 s spreading value, $s$	5	10	25
Peak steepness [%]	1	2	4

Table 2  
Directional sensitivity tests (10 tests in total).

Wave parameter	Range of value(s)
Peak frequency, $f_p$ [Hz]	0.6
cos-2 s spreading value, $s$	10
Peak steepness [%]	2
Mean direction, $\theta$ [deg]	18, 36, 54, ..., 180

the method performance. Finally three complex sea states were created, using combinations of parametric seas to provide unconventional wave conditions; both multi-modal and highly spread. The wave parameters for these sea states are shown in Tables 1, 2 and 3.

The complex sea states in Table 3 have been designed to prove that the method can reconstruct such spectra, whilst additionally isolating the incident and reflected components over 360°. The first spectrum is a multi-modal sea state consisting of two identical wave systems with the mean direction 120° apart, whilst the second spectrum is a single wave system with a very large directional spread, spanning 360°. Two completely opposing wave systems have been used for spectrum three, with a slight difference in peak frequency. These spectra are illustrated in Fig. 17. It is often difficult to isolate the different incident modes of such spectra using conventional methods, and the isolation of the incident and reflected spectra is not usually possible at all without a defined incident range. These tests therefore serve as a useful demonstration of the capability of the SPAIR approach used here.

#### 2.1.2. Wave generation

Deterministic waves are generated at FloWave using force-feedback wavemakers, providing a very high degree of repeatability (Ingram et al., 2014). This enables device alterations to be assessed independently of sea state variations, and allows wave-by-wave comparisons to be made of the device in the time domain.

Throughout this work the generation of directional wave spectra is achieved using the single-summation method, avoiding phase-locking (Miles and Funke, 1989). Phase-locking occurs when waves at the same frequency but different directions interact, causing spatial patterns across the tank, thus creating a non-ergodic wave field. To avoid this, the initial frequency increments,  $\Delta F$ , can be split up further to create sub-frequency increments  $\delta f = \Delta F/N_\theta$ , as shown in Pascal (2012). These new frequency increments, still within the original frequency bins, now have a unique wave propagation direction associated with each of them. In addition to avoiding phase-locking, this method of wave generation is key to the application of the SPAIR method. This generation approach is demonstrated in Fig. 2.

Using the re-defined directional spectrum, the surface elevation can be calculated via an Inverse Fast Fourier Transform (IFFT), or summation. The surface elevation at point  $[x,y]$ , and time  $t$  can now be described by:

$$\eta(x, y, t) = \sum_{i=0}^{N_f \cdot N_\theta - 1} A_i \cos(-\omega_i t + k_i [x \cos \alpha_i + y \sin \alpha_i] + \Phi_i) \quad (1)$$

where:

- $A_i$  wave amplitude of frequency component  $i$
- $\omega_i$  angular frequency of component  $i$ , rad/s
- $k_i = \frac{2\pi}{L_i}$ , wavenumber of component  $i$

Table 3  
Complex spectra tests.

Wave parameter	Spec 1	Spec 2	Spec 3
Peak frequency, $f_p$ [Hz]	0.5, 0.5	0.45	0.45, 0.55
cos-2 s spreading value, $s$	5, 5	0.5	20, 20
Mean direction, $\theta$ [deg]	45, 165	120	90, 270

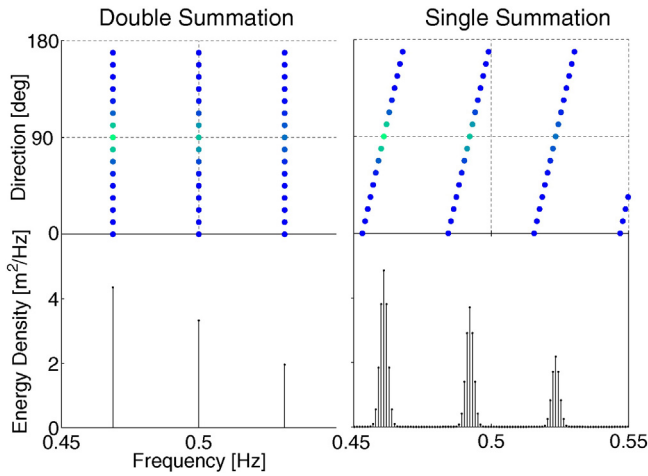


Fig. 2. The single (right) and double (left) summation methods of wave generation. This demonstrates how wave partitions made in the frequency domain are attributed unique directions (Draycott et al., 2015).

$\alpha_i$  wave direction of component  $i$   
 $\Phi_i$  phase of component  $i$  at  $x = y = t = 0$ .

The sea states presented here have a repeat time,  $T$ , of 1024 s. This defines the frequency increments,  $\delta f$ , to be  $\frac{1}{1024}$  Hz, providing 2048 frequency components within the tank’s nominal generation range, 0–2 Hz. For the simulation of directional spectra this was achieved using 64 frequency bins, and 32 directional bins ( $N_f = 64, N_\theta = 32$ ). Re-defining the directional spectrum for use in the single-summation method gives the required frequency increments of:

$$\delta f = \frac{\Delta F}{N_\theta} = \frac{f_{max}}{(N_f \times N_\theta)} = \frac{1}{T} = \frac{1}{1024} [\text{Hz}] \quad (2)$$

2.2. Experimental configuration

Wave surface elevations are measured within the facility using multiplexed two-wire resistance type wave gauges, each providing a point measurement with a sample frequency of 32 Hz. The wave generation and data acquisition (DAQ) are synchronised using a common clock, and are controlled using a single interface provided by Edinburgh Designs. Such synchronisation of DAQ and wavemaker system is expected to be needed for the application of the new method.

In order to estimate wave directionality these gauges must be deployed in an array. The wave directions will be inferred from the known array spacings, and as such it is important that these vector separations cover as many directions and magnitudes as possible relative to the wavelengths present in the tank. For DSF-based reconstruction methods this enables the directional distributions to be inferred at a range of frequencies with greater angular resolution. The PTPD method detailed in Section 2.3.1 only requires a minimum of 3 gauges, however a larger number of vector separations enables effective error reduction (see Fig. 8). In addition to this, the reflection analysis procedure shown in Section 2.3.2 benefits from having a range of projected in-line array separations for each calculated direction.

Inter-array gauge separations can be represented by their co-array, describing the vector separations between all points (Haubrich, 1968). Effective directional wave gauge arrays therefore have a uniform co-array, spanning the appropriate range of magnitudes. With this criteria in mind, an 8 gauge array layout was designed for installation on a re-configurable rig, shown in Fig. 3, with the co-array and projected in-line separations shown in Figs. 4 and 5 respectively.

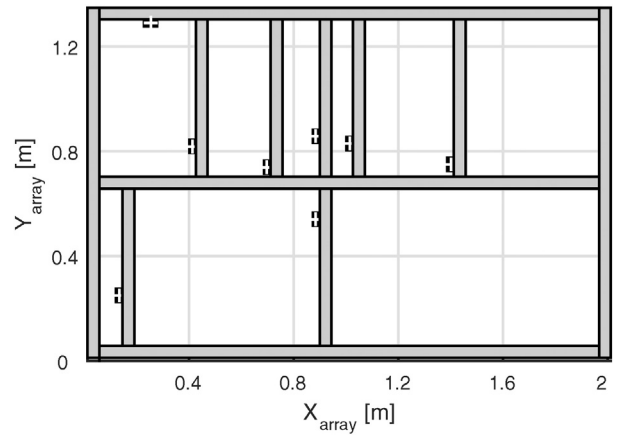


Fig. 3. Wave gauge array layout with bar positions for re-configurable rig.

It is observed that the co-array of the array design is largely uniform with no duplicate vector separations, and that there is a good range of projected in-line separations for every angle of incidence. The size of the array was chosen to ensure that there is a sufficient number of useful separations for the frequency range of interest, taken here to be 0.2 – 1.2 Hz. Analogous to the criteria proposed by Goda and Suzuki (1976) for reflection analysis, separations are considered useful for frequency component  $i$  if they are between  $0.05\lambda_i$  and  $0.45\lambda_i$ . As  $\lambda_f = 1.2$  Hz is 1.08 m, and  $\lambda_f = 0.2$  Hz is roughly 21 m, the array has been designed so that there are a sufficient number of separations smaller than 0.49 m and larger than 1.05 m.

Gauges are used in groups of three to estimate wave angles, and so for a given frequency component the estimate is only assumed valid if all separations adhere to the separation criteria. The resulting number of valid gauge triads as a function of frequency is shown in Fig. 6, and it can be seen that for the frequency components of interest there are normally multiple useful gauge triads, and hence multiple valid angle estimates.

2.3. The SPAIR method applied to the FloWave Ocean Energy Research Facility

The SPAIR method as detailed in this section uses single-summation wave generation before estimating the frequency dependent incident angles. These angles provide projected in-line separations, which are used to perform a 2D reflection analysis for each frequency component. Under the assumption that this frequency dependent 2D approach is

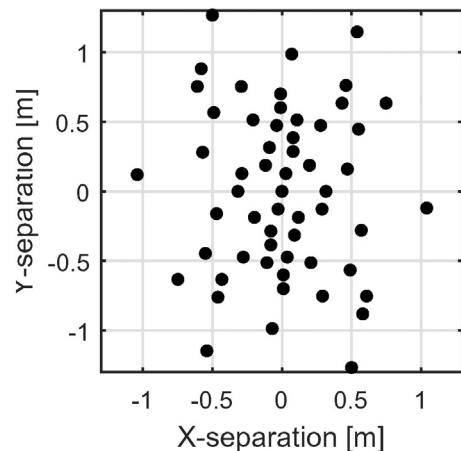


Fig. 4. Co-array separations for the wave gauge array layout shown in Fig. 3.



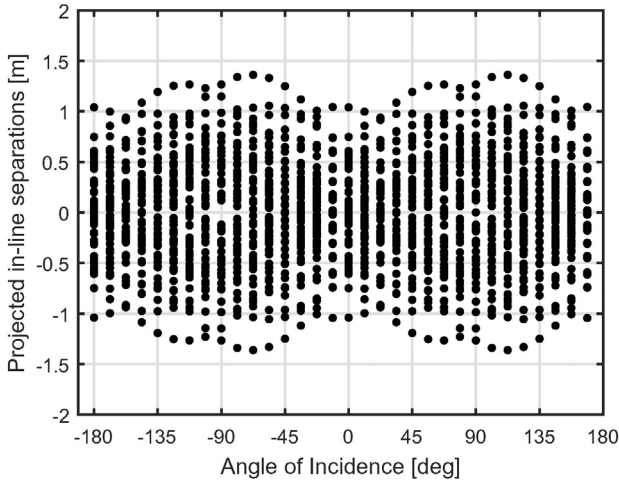


Fig. 5. Projected in-line wave gauge separations for a range of angles of incidence.

valid, this enables isolation of the incident and reflected directional spectra, and time-series.

The complete method works very well for sea state validation at the FloWave Ocean Energy Research Facility. However, the combined use of all the single-summation based tools present in the SPAIR method may not always be appropriate. For example, if it is known that the wave tank produces incident waves at the correct angle then the initial PTPD angle calculation is not required. Also if reflections are large, and not a mirror of the incident, the reflection analysis procedure will give unreliable results. The method limitations and sensitivity are detailed in Section 4.1, and alternative uses of the tools are discussed in Section 4.2.

2.3.1. Input angle calculation using PTPD approach

The current methods of calculating directional spectra in tanks, such as the EMEP and BDM approaches, have been developed for ocean measurement and subsequently utilised for wave tank analysis. Similarly, the PTPD approach was also initially developed for use in ocean measurement (Esteva, 1976; Fernandes et al., 2000). This technique has not however made the transition to the tank environment for the routine reconstruction of directional spectra. This is likely because of the method's inability to effectively resolve directional spectra in the ocean.

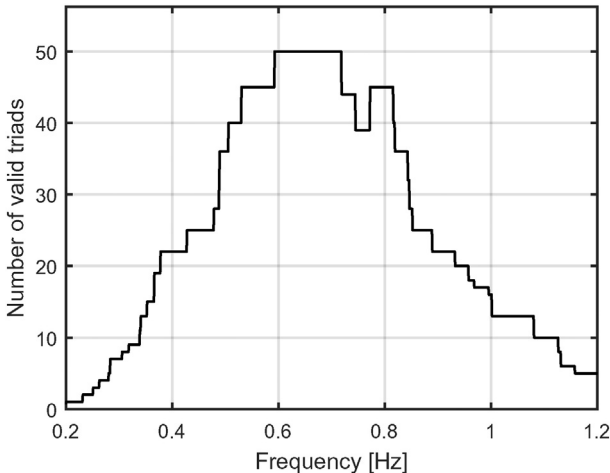


Fig. 6. Number of valid gauge triads (all separations >0.05λ<sub>i</sub> and <0.45λ<sub>i</sub>) as a function of frequency for the array shown in Fig. 3.

The PTPD approach uses the phase difference between triads of gauges to infer the wave direction. In the ocean, and when using the double-summation method in tanks, the phase differences at a given frequency will encompass a range of wave components travelling in different directions. In practice the result is that the PTPD outputs essentially give a representative angle for that frequency band and cannot be used to create a full directional spectrum. When using the single-summation method of wave generation, however, there are many discrete frequency components, each of which propagates in a single direction. This should enable the method to calculate the actual directions at each sub-frequency, thereby allowing effective reconstruction of a directional spectrum when re-considering the desired, original frequency bins.

The present work uses 8 wave gauges to improve the propagation direction estimate, as previously described by Draycott et al. (2015). The method is implemented as follows:

1. Obtain Fourier coefficients  $a_{i,n}$  using an FFT for each gauge  $n$ . Calculate amplitudes  $A_{i,n}$  and absolute phases  $\Phi_{i,n}$ .
2. Find all 3 gauge combinations for  $N$  gauges, i.e.  ${}^8C_3 = 56$ . For every triad and all frequency components:
3. Ensure relative separations  $L_{1,2}$ ,  $L_{1,3}$  and  $L_{2,3}$  are all  $>0.05\lambda_i(f)$  and  $<0.45\lambda_i(f)$ . If so:
4. Calculate relative phases  $\Phi_{1,2}$  and  $\Phi_{1,3}$ .
5. Calculate perceived angle,  $\alpha$ , by the method of Esteva (1976). The final equations of which are shown below:

$$\alpha = \tan^{-1} \frac{[(x_1 - x_2)\Phi_{1,3} - (x_1 - x_3)\Phi_{1,2}]/\text{sgn}(P)}{[(y_1 - y_3)\Phi_{1,2} - (y_1 - y_2)\Phi_{1,3}]/\text{sgn}(P)} \tag{3}$$

$$P = [(x_1 - x_2)(y_1 - y_3) - (x_1 - x_3)(y_1 - y_2)]. \tag{4}$$

6. Take the peak of a circular kernel density estimate over all valid triad combinations as the propagation direction for that frequency.
7. Comparisons can now be made between the desired and measured angles, as per the single summation method. Additionally the data can be re-binned and compared with the desired directional spectrum.

The PTPD approach relies on the fact that the phase difference between gauges is a function of the frequency-dependent wavelength and their relative positions. The phase difference between gauge  $n$  and gauge  $m$ , for a given Fourier coefficient,  $i$ , can therefore be represented as:

$$\begin{aligned} \Phi_{i,nm} &= k_i[(x_n - x_m) \cos\alpha_i + (y_n - y_m) \sin\alpha_i] \\ &= k_i(x'_{i,n} - x'_{i,m}). \end{aligned} \tag{5}$$

Fig. 7 shows the projected in-line x-positions for frequency  $i$ ,  $x_{i,n}$ , as a function of the measured wave direction,  $\alpha_i$ . Although only 3 gauges are required to get an estimate of the wave directions it is advantageous to have multiple estimates for the propagation direction at each frequency. This is because measurement noise, position error and the presence, or build-up of reflections, may result in errors in individual directional estimates.

In this work a maximum of 56 estimates are used to give a representative direction for each frequency, disregarding estimates derived from triads with inappropriate separation magnitudes. A circular mean, or circular median value may be used from these to estimate the true incident direction at this frequency, however, to limit the influence from rogue estimates a circular kernel density estimate has been used for this work. The peak of this kernel density estimate should generally represent the



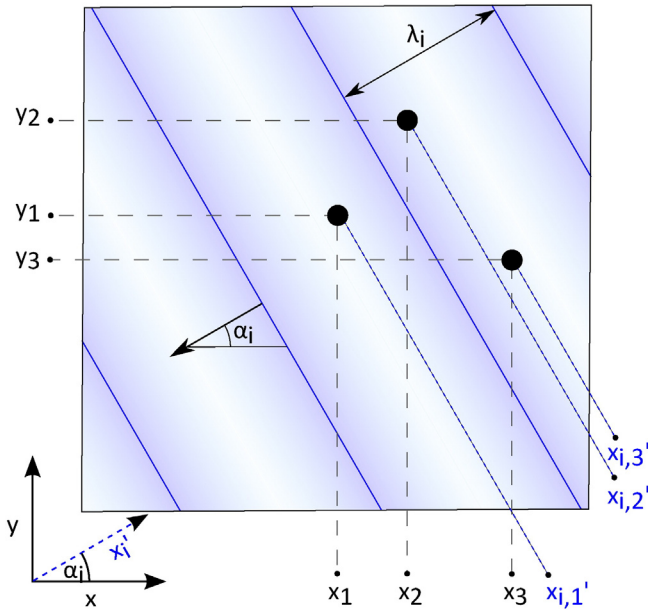


Fig. 7. Example projected x values for a single frequency component and its associated propagation direction.

incident wave direction, with estimates lying either side of the peak being affected more strongly by reflections or position error etc.

There are 2048 kernel density estimates for each sea state, corresponding to the discrete frequency increments used in these tests. Fig. 8 shows some example outputs of these estimates, highlighting the requirement to have multiple estimates in some scenarios, but not others. Fig. 8a and d highlights the advantage of using the peak of the kernel density estimates, rather than the mean, with Fig. 8a

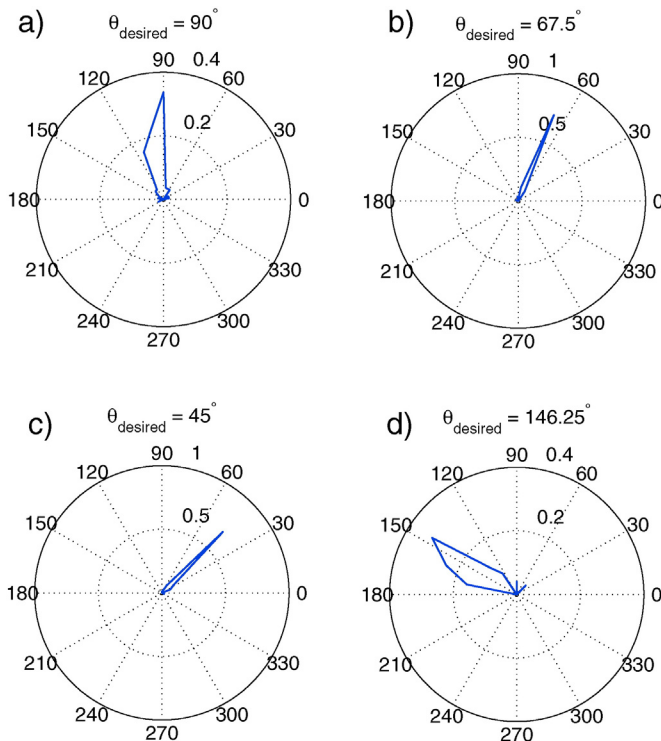


Fig. 8. Example circular kernel density outputs showing a range of different spreads in the estimate.

demonstrating this particularly well. It is clear here that using the circular mean value would have lead to a significant ‘over-estimate’ of the wave direction, amounting to around 10°.

2.3.2. Calculating in-line reflections using projected gauge positions

The PTPD approach used here takes advantage of the fact that the phase differences at a given frequency should be solely a function of the gauge positions and the wave propagation direction. This trait allows for the calculation of frequency dependent, in-line separations:

$$x'_{i,n} - x'_{i,m} = (x_n - x_m) \cos \alpha_i + (y_n - y_m) \sin \alpha_i. \quad (6)$$

The complex amplitude spectra measured at each gauge,  $a_{i,n}$ , along with these assumed separations then allow a reflection analysis procedure to take place. The process in doing this essentially treats each frequency component as a uni-directional problem.

Typical uni-directional reflection analysis can be achieved with a small number of gauges, as demonstrated by Goda and Suzuki (1976) for 2 gauges, and Mansard and Funke (1980), using a least-squares approach with 3 gauges. These methods require the gauge separations to be within a small range to give useful estimates. In this multi-directional work the effective in-line separations are highly variable, and as such require more gauges to ensure useful spacings are available.

Zelt and Skjelbreia (1992) present an extension to the Mansard & Funke method, formulating a weighted least-square approach to estimating incident and reflected wave fields for any number of gauges. This approach is used in this work with some slight modification. The three modifications made are as follows:

1. x-Values are now frequency dependent in-line x-positions, based on the calculated  $\alpha$  values.
2. Absolute phases are used rather than phase difference to gauge 1. This eventually allows reconstruction of total, incident, and reflected time-series, and also direct use of the isolated Fourier coefficients.
3. As a weighting function the goodness function presented in Zelt and Skjelbreia (1992) is used in conjunction with the coherence spectra between gauges (dot product). This should enable spacing considerations (goodness function) to be considered in conjunction with a measure of the consistency of the phase differences between gauges. In the results presented here this has made little improvement (<2%). If, however there are particularly noisy signals, or if complex reflections build up throughout a test this may prove more useful. The coherence spectra were calculated using the in-built mscohere MATLAB function.

The final modified equations used to calculate the complex incident and reflected Fourier coefficients,  $a_{inc}$  and  $a_{ref}$  are shown below:

$$a_{inc,i} = \sum_{n=1}^N C_{i,n} a_{i,n} \quad (7)$$

$$a_{ref,i} = \sum_{n=1}^N C_{i,n}^* a_{i,n} \quad (8)$$

where  $a_{i,n}$  is the measured Fourier coefficients with absolute phase (rather than with phases relative to gauge 1), and

$$C_{i,n} = \frac{2iW_{i,n}}{D} \sum_{m=1}^N W_{i,m} \sin(\Delta\Phi_{i,mm}) e^{i\Phi_{i,m}} \quad (9)$$

$$D = 4 \sum_{n=1}^N \sum_{m < n} W_{i,n} W_{i,m} [\sin(\Delta\Phi_{i,mm})]^2 \quad (10)$$

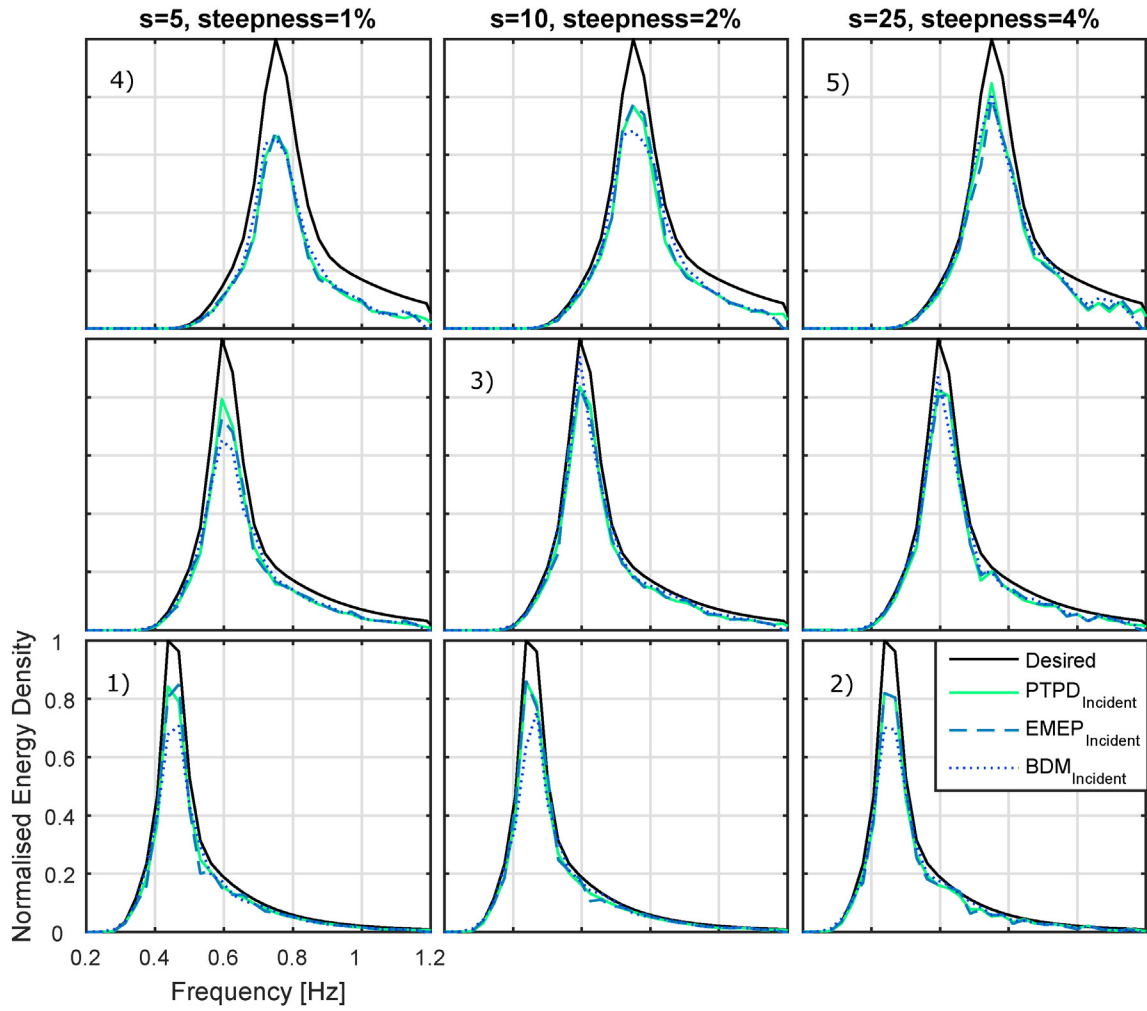


Fig. 9. Example frequency spectra outputs with numbers corresponding to directional spectra in Fig. 10.

where:

$$\Delta\Phi_{i,nm} = k_i[(x_n - x_m) \cos\alpha_i + (y_n - y_m) \sin\alpha_i] = k_i(x'_{i,n} - x'_{i,m}) \quad (11)$$

$$\Phi_{i,m} = k_i \cdot x'_{i,m}. \quad (12)$$

$W_{i,n}$  is the weighting function for gauge  $n$  and frequency  $i$ . See Zelt and Skjelbreia (1992) for the goodness function, and Mandel and Wolf (1976) for information on coherence spectra.

These equations allow the incident and reflected amplitude spectra to be resolved for single-summation generated directional spectrum. The incident and reflected wave energy density spectra can now be calculated as:

$$S_{inc,i} = \frac{|a_{inc,i}|^2}{2 \cdot \delta f} \quad (13)$$

$$S_{ref,i} = \frac{|a_{ref,i}|^2}{2 \cdot \delta f}. \quad (14)$$

The frequency-dependent reflection coefficient,  $K_{r,i}$ , can also be readily calculated as:

$$K_{r,i} = \frac{|a_{ref,i}|}{|a_{inc,i}|}. \quad (15)$$

### 2.3.3. Calculating the updated incident, and the reflected directional spectrum

Knowledge of the incident and reflected wave frequency spectrum does not allow for an update to be made to the incident directional spectrum directly. The reflections present in the tank cause gauge dependent amplitude and phase deviations. The nature of the PTPD approach means that these can manifest themselves as a directional distribution error, rather than being isolated. This requires the incident propagation directions to be recalculated, using the already isolated incident Fourier coefficients.

In order to fix the measured incident directional spectrum the isolated incident Fourier coefficients can be re-processed using the PTPD approach. This requires the phases for the base Fourier coefficients,  $a_{inc,i}$ , at  $[0,0]$ , to be shifted to the in-line apparent gauge positions. This is done noting that:

$$a_{i,n} = a_{inc,i} e^{-i\Phi_{i,n}} + a_{ref,i} e^{i\Phi_{i,n}}. \quad (16)$$

This defines the incident, position shifted Fourier coefficients as:

$$a_{inc,i,n} = a_{inc,i} e^{-i\Phi_{i,n}} = a_{inc,i} e^{-i(k_i x'_{i,n})}. \quad (17)$$

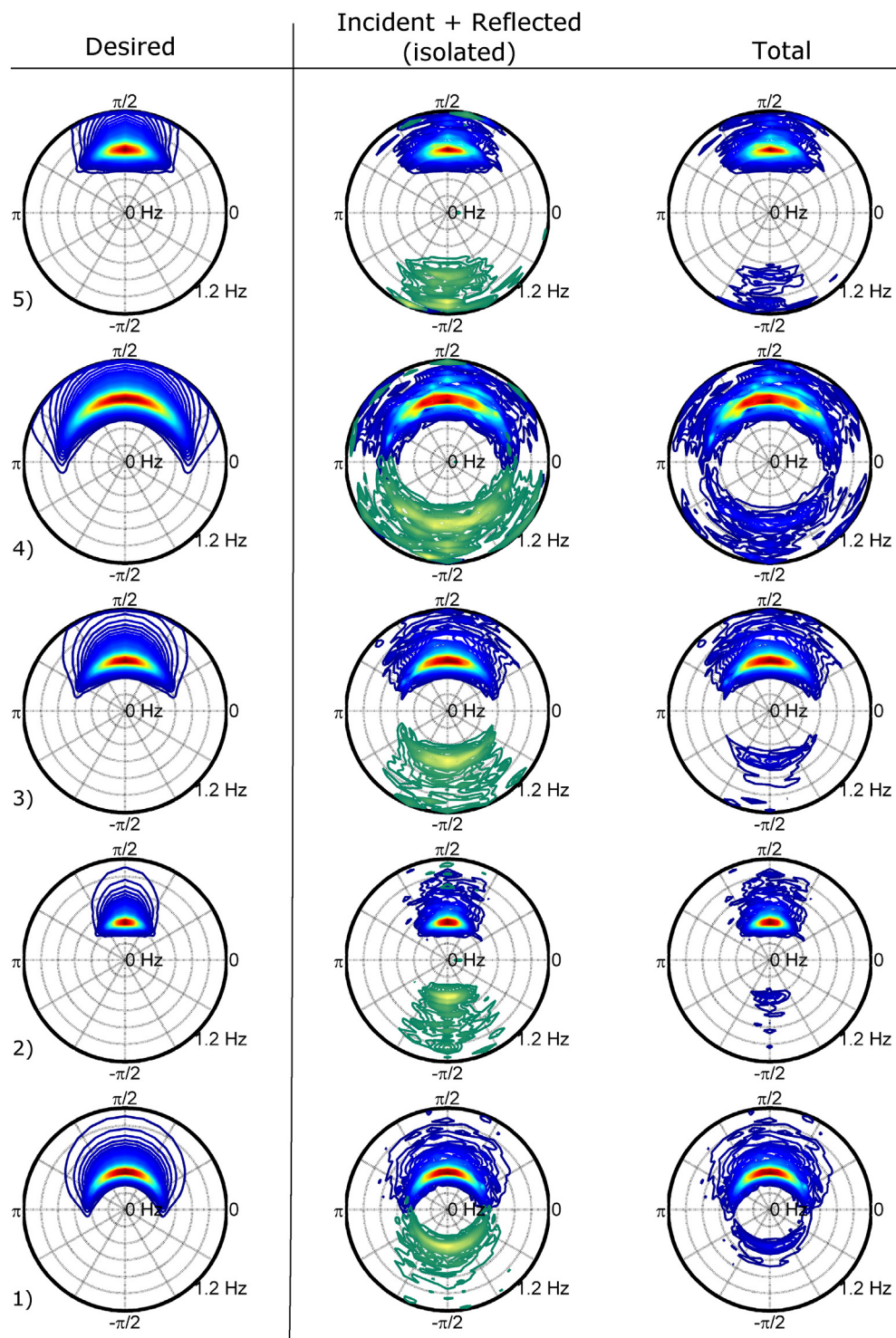


**Fig. 10.** Example SPAIR reconstructed directional spectra outputs. Energy density [ $\text{m}^2/\text{s}/\text{rad}$ ] is shown by the colour, relative to the peak of the desired spectrum. 1) 0.45 Hz,  $s = 5$ ,  $st = 1\%$ , 2) 0.45 Hz,  $s = 25$ ,  $st = 4\%$ , 3) 0.6 Hz,  $s = 10$ ,  $st = 2\%$  4) 0.75 Hz,  $s = 5$ ,  $st = 1\%$  5) 0.75 Hz,  $s = 25$ ,  $st = 4\%$ . (For interpretation of the references to colour in this figure legend, the reader is referred to the web version of this article.)

These Fourier coefficients can now be used directly with the PTPD approach, enabling an estimate of the incident directional spectrum to be made with an attempt to remove the artificial amplitude and phase deviations. The reflected directional spectrum can be calculated similarly, or more easily through knowledge of the reflection coefficients. In

addition to this, the incident and reflected time series at the gauge positions can be estimated through an IFFT.

The nature of this combined approach means that incident and reflected spectra can be separated over all directions without requiring prior knowledge of the input angular range. Neither the BDM or EMEP



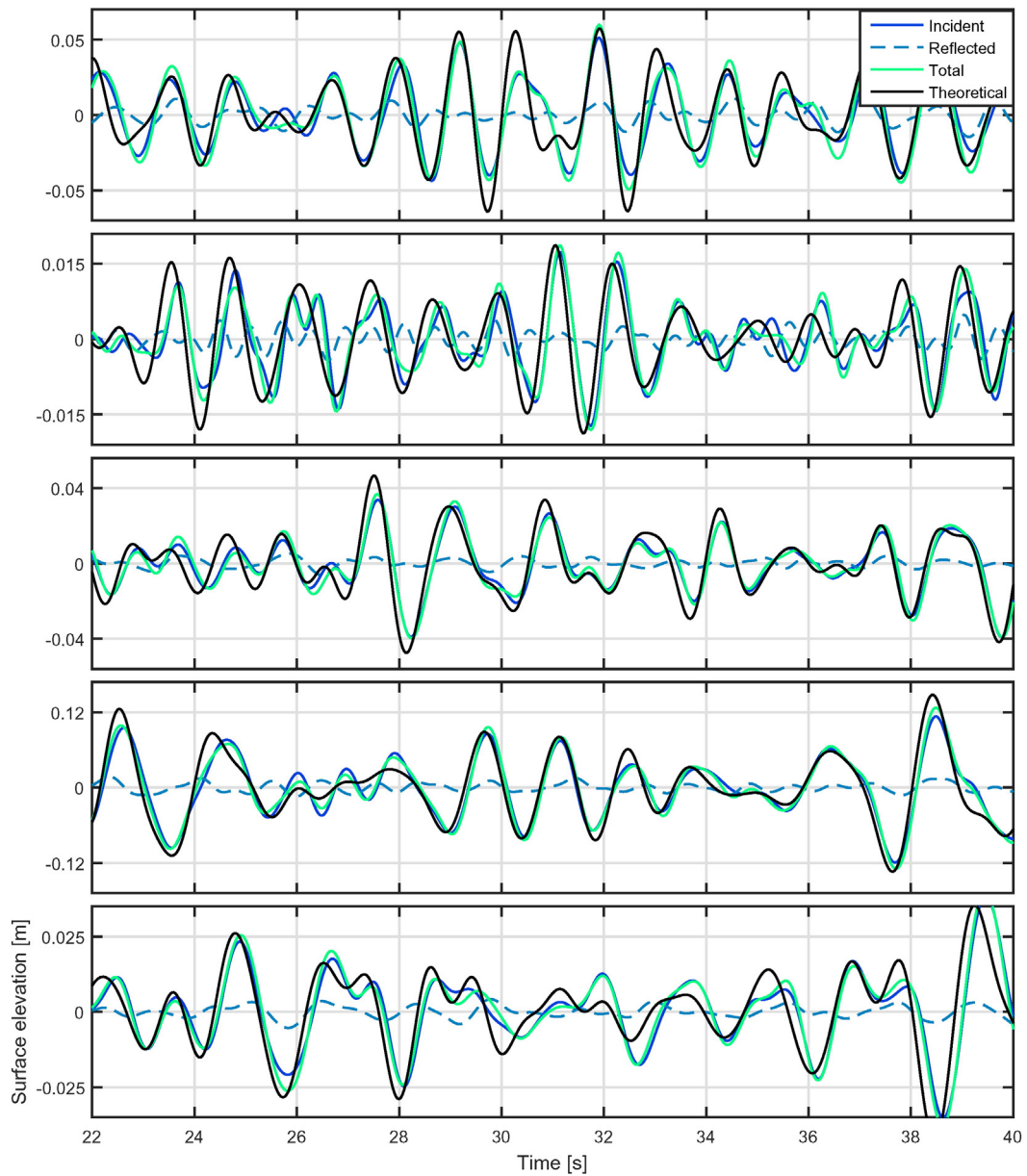


Fig. 11. Example time series outputs for the example spectra shown in Figs. 9 and 10. Theoretical time series as well as measured are shown, in addition to the isolated incident and reflected components for a range of gauges. Sea state 1, gauge 1; sea state 2, gauge 2 etc.

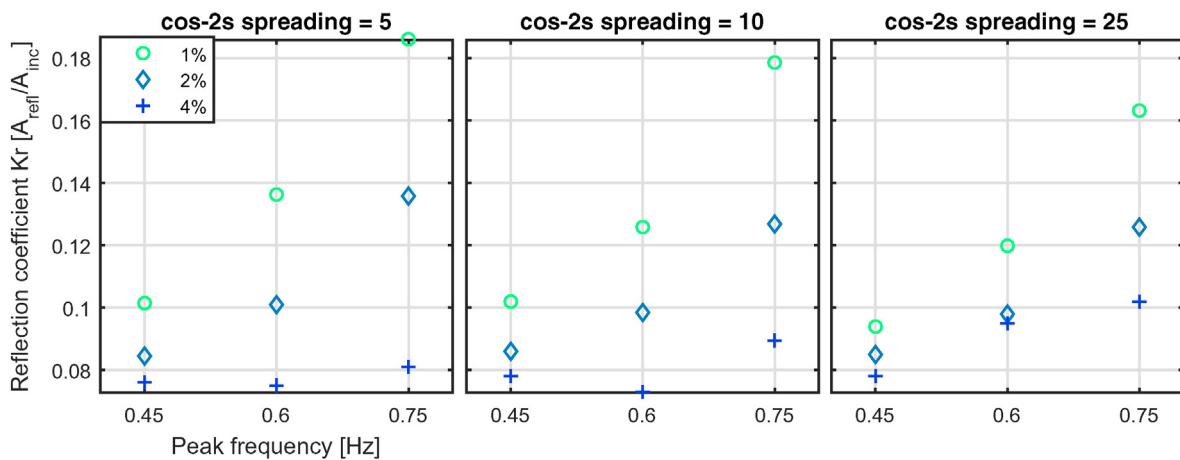
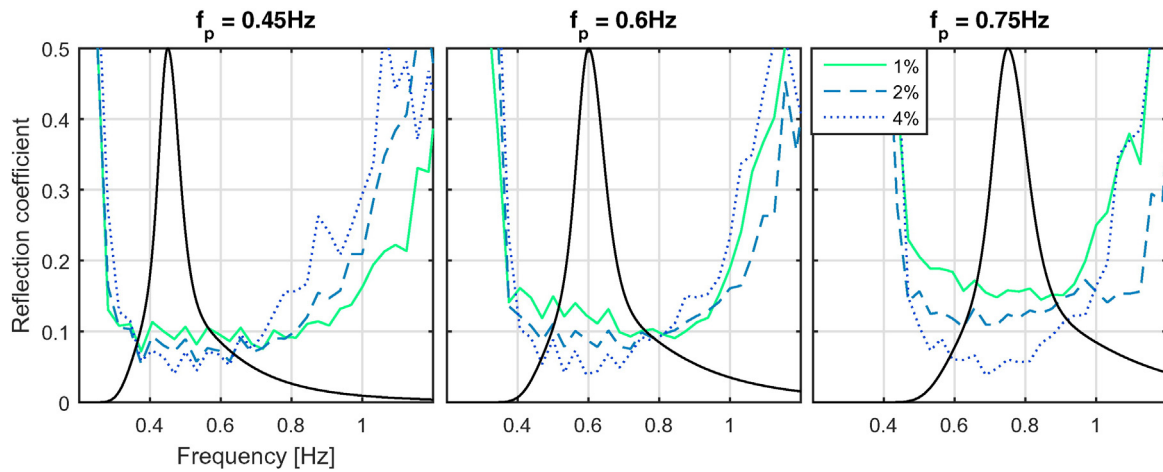


Fig. 12. Overall reflection coefficients for different values of spreading, peak frequency, and wave steepness.



**Fig. 13.** Mean frequency dependent reflection coefficients for each peak frequency averaged over directional spreading, separated by steepness. Normalised wave spectra overlaid to aid explanation of overall reflection coefficients (Fig. 12).

approaches are capable of achieving this, and even with a defined input range are shown to exhibit much larger uncertainties.

### 3. Results

#### 3.1. Frequency spectra

Example incident frequency spectra are shown in Fig. 9. These provide results for a range of sea states covering both the highest and lowest reflection conditions, as shown in Fig. 12. There is an apparent tendency to under-produce waves, particularly at the spectral peak, and whilst being more pronounced for sea states with higher peak frequency, and inherently higher reflections, it is prevalent throughout. In general the deviation is much lower for sea states with lower peak frequency, suggesting that, as expected, the tank's generating and absorbing effectiveness reduces above a certain frequency threshold. To demonstrate that this deviation isn't a function of the method, and to allow comparisons to be made in Section 3.5.1, the frequency spectra outputs for the BDM and EMEP approaches are also been shown.

This deviation, despite being consistent, is also easy to rectify. Linear frequency dependent correction factors can be applied as a function of the deviation between the target amplitude spectrum and the isolated incident spectrum. These have proved to be effective in previous tests, bringing down the relative deviation to 1 – 2%. As the current tests are

focussed on directional distribution and reflection calculation it was not deemed necessary to apply them for this purpose.

#### 3.2. Incident and reflected directional spectra

Directional spectra relating to the numbered frequency spectra in Fig. 9 are shown in Fig. 10, ensuring the extremes of the test programme are still included. The majority of sea states shows good agreement between the input and measured spectra. The difference between the measured incident spectrum from the desired input is generally low, with the exception of sea state 4. Viewing the colour-scale-separated spectra (middle column of Fig. 10) it is apparent that the reflected spectrum has been effectively isolated, generally mirroring the form of the incident distribution.

It is apparent that example sea state 4 demonstrates much larger deviations than the others. Fig. 9 highlights that this is largely due to significant under-generation, whilst in Fig. 12 it is observed that the reflection coefficient is also very high. This re-iterates the findings that high frequency, low amplitude waves are generated, and absorbed less effectively, especially when combined with high directional spreading.

#### 3.3. Time series

Fig. 11 shows the example time series outputs for the spectra in Fig. 10. An IFFT of the complex input amplitude spectra enables the

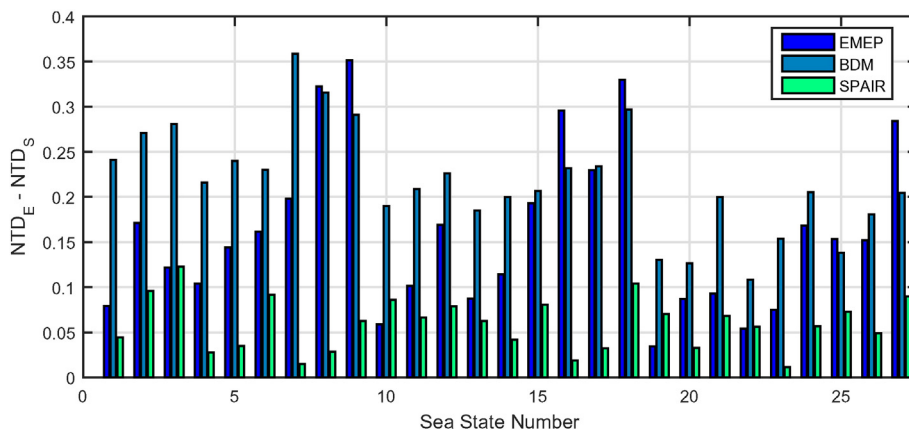


**Fig. 14.** Comparison of directional distribution error for calculated incident spectra created using the EMEP, BDM and SPAIR approaches.

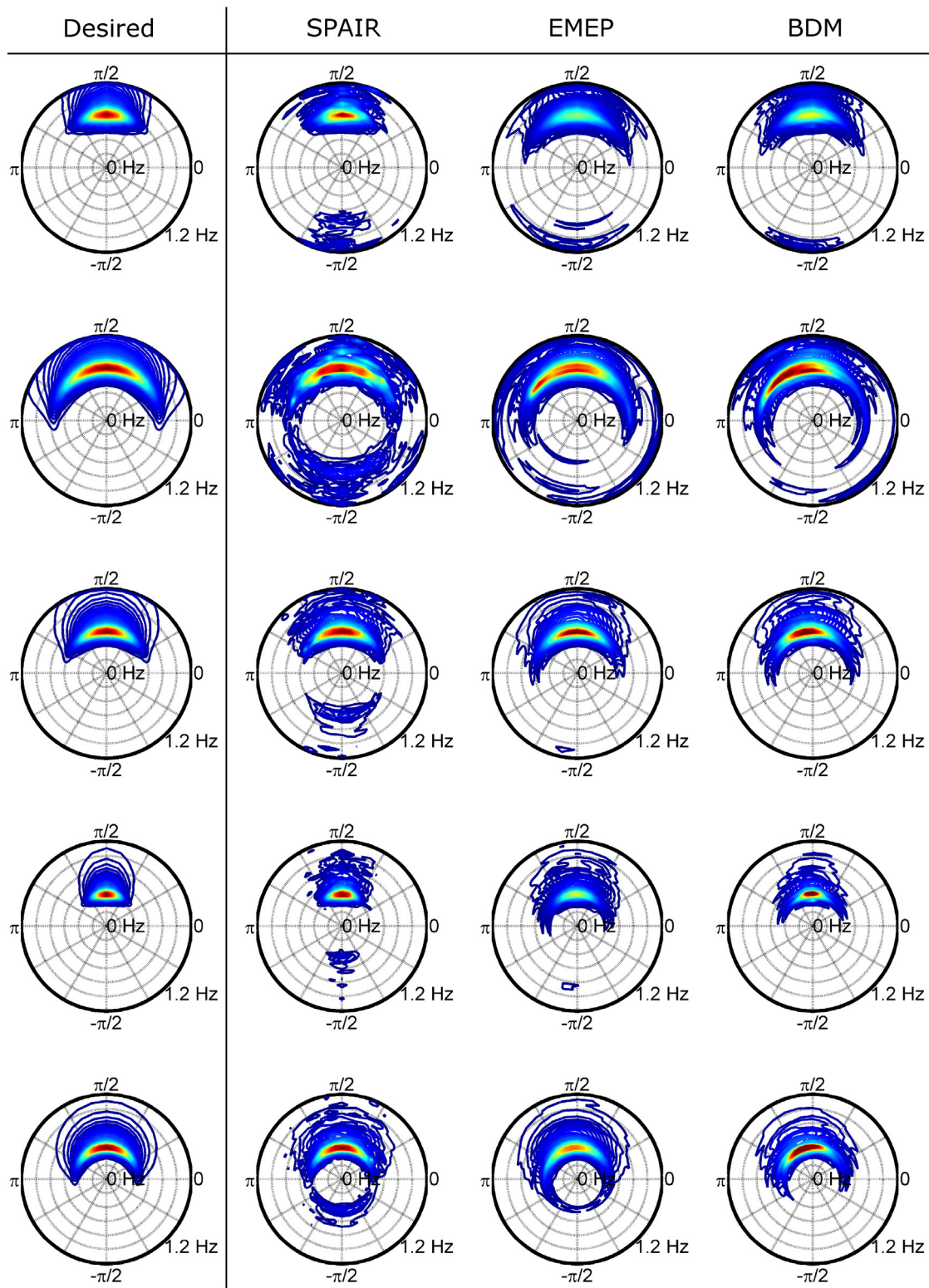
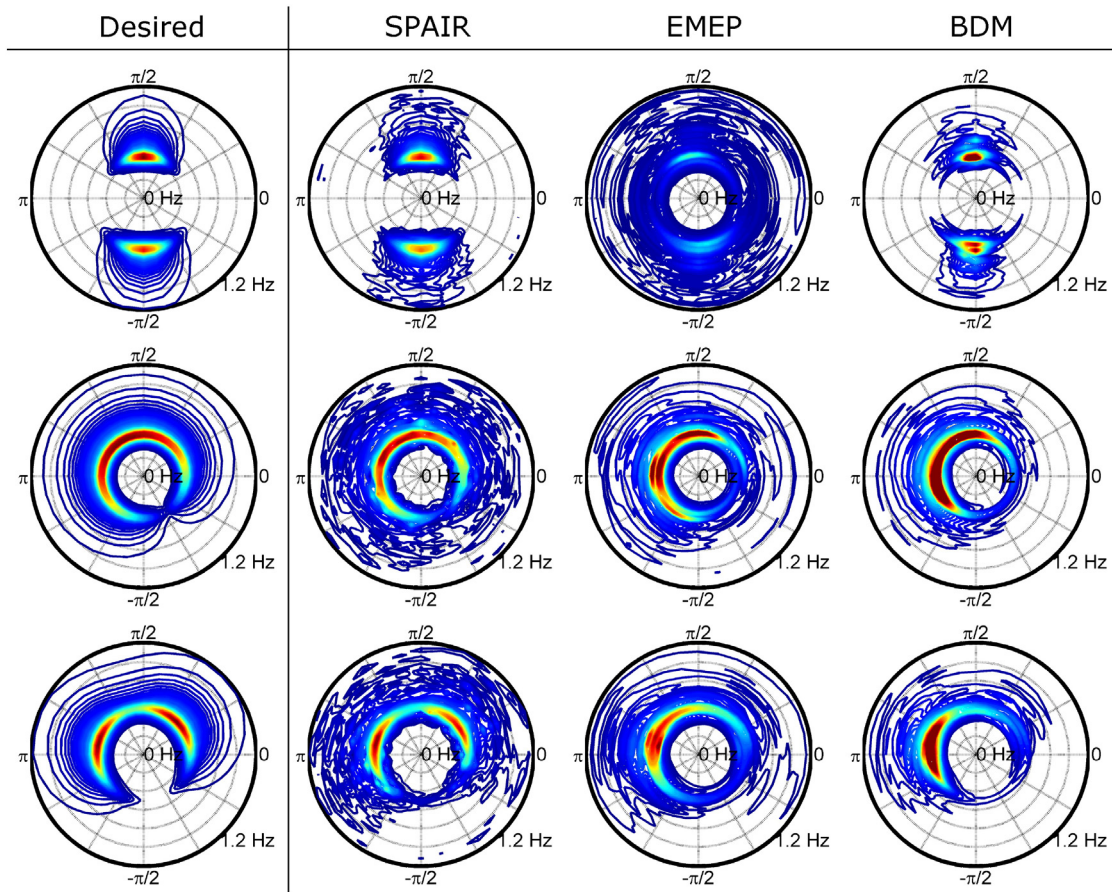


Fig. 15. Comparison of example directional spectrum outputs from SPAIR, EMEP and BDM approaches. Energy density [ $\text{m}^2\text{s}/\text{rad}$ ] is shown by the colour, relative to the peak of the desired spectrum. (For interpretation of the references to colour in this figure legend, the reader is referred to the web version of this article.)

theoretical time series to be computed using linear wave theory, before being compared to the actual measurements. As shown in Section 2.3.3, the presented method also allows for the separation of incident and reflected time series in the tank domain, and as such these have been computed at the gauge locations for comparison.

The measured time series outputs show reasonably good agreement with the theoretical time series calculated using linear wave theory. The removal of the reflected components generally provides a closer match, however, this is not always the case. The isolation of what is unaccounted reflections from non-linear behaviour appears difficult. As expected from





**Fig. 16.** Complex directional spectra outputs (total) for SPAIR, BDM and EMEP approaches. Energy density [ $\text{m}^2/\text{s}/\text{rad}$ ] is shown by the colour, relative to the peak of the desired spectrum. (For interpretation of the references to colour in this figure legend, the reader is referred to the web version of this article.)

the spectral analysis, example sea state 4 shows the largest deviations, and also the largest relative reflected components.

### 3.4. Reflection analysis

The output of the directional reflection analysis for the  $3 \times 3 \times 3$  test matrix is shown in Fig. 12. Reflections in the FloWave facility are primarily related to the absorption characteristics of the force-feedback wavemakers, and as such are both frequency and amplitude dependent. This is demonstrated in Fig. 12 where it can be clearly observed that increasing peak frequency, or decreasing wave steepness, causes an increase in the overall wave reflection coefficient. This frequency dependency can be attributed to the paddle characteristics, as well as absorption control scheme, as explored in Gyongy et al. (2014). The reduced sensitivity of the force-feedback mechanism to low wave forces appears to drive the decreased absorption effectiveness for small, low steepness waves.

Fig. 13 shows the mean frequency dependent reflection coefficients for each peak frequency used, averaged over directional spreading. This enables a more detailed frequency dependent exploration of the reflection coefficients, and offers further explanation to the results shown in Fig. 12.

### 3.5. Method performance

#### 3.5.1. Comparison to other methods

In order to assess combined sea state and method performance, the Normalised Total Difference (NTD) between target and measured spectra can be assessed, defined as:

For directional spectra:

$$NTD_E = \frac{\sum_{p=1}^{N_f} \sum_{q=1}^{N_\theta} |E_{i,pq} - E_{m,pq}|}{\sum_{p=1}^{N_f} \sum_{q=1}^{N_\theta} E_{i,pq}} \quad (18)$$

For frequency spectra:

$$NTD_S = \frac{\sum_{p=1}^{N_f} |S_{i,p} - S_{m,p}|}{\sum_{p=1}^{N_f} S_{i,p}} \quad (19)$$

$NTD_E$  provides assessment of the total deviation from target spectra, which includes:

- frequency spectrum error,  $NTD_S$
- directional distribution error,  $NTD_D$
- method reconstruction error,  $NTD_M$
- miscellaneous (other) error,  $NTD_O$  e.g. noise, position error.

Ideally the method reconstruction error,  $NTD_M$ , would be assessed to gauge method performance. It is not possible, however, to isolate this as the true directional distribution error is not known. Fig. 9 shows that the deviation from target frequency spectra,  $NTD_S$ , is mostly tank dependent and not a function of the methodology. For these reasons to assess method performance,  $NTD_E - NTD_S$  has been used, noting that it incorporates the method reconstruction error, along with the directional distribution error. As the true distribution error is constant this should allow effective comparisons to be made between methods.

Fig. 14 shows this comparison for the calculated incident spectra (using a fixed input range of  $0-180^\circ$  for BDM and EMEP methods)

**Table 4**  
Directional distribution error,  $NTD_E - NTD_S$ , for complex spectra.

$NTD_E - NTD_S$	Sea state 1	Sea state 2	Sea state 3
SPAIR	0.153	0.127	0.054
EMEP	0.340	0.227	0.454
BDM	0.414	0.344	0.322

over the initial  $3 \times 3 \times 3$  test plan. The SPAIR approach consistently performs better, with a mean NTD of 5.93%, compared with 16.1 and 21.7% for the EMEP and BDM approaches respectively.

Example directional spectrum outputs from these methods are shown in Fig. 15, for the same sea states as shown in Fig. 10. It can be seen that neither the EMEP or BDM approaches consistently fit a DSF that incorporates reflected components. The EMEP approach appears to incorporate some reflected energy content, but the distribution seems incorrect, likely constrained by the inherent frequency-dependent ‘curve-fitting’ process.

Visually all of the methods perform reasonably well in terms of characterising the incident wave field, with the SPAIR approach demonstrating the best performance, as shown in Fig. 14. This is also apparent through visual observation, as the high energy components of the incident distribution match up very well with that of the desired. At low energy levels, however, the distribution does appear to be ill-defined, a function of the discretised nature of the solution, and the low energy densities present at these frequencies.

### 3.5.2. Performance with complex spectra

The complex spectra defined in Table 3 have no defined incident and reflected range and as such the EMEP and BDM approaches cannot

resolve the reflected components. Fig. 16 shows the total reconstructed wave field using the three methodologies. It is clear that the EMEP and BDM approaches generally fail to capture the multi-modal and highly spread nature of the input sea states, other than perhaps the BDM approach reconstruction of sea state 3.

The SPAIR approach enables a much more effective characterisation of the input conditions, as demonstrated in Fig. 16 and Table 4. The reflected spectrum and coefficients can also be calculated as no input angular range is required, with the result that the incident and reflected spectra can apparently overlap. The reflected spectra are shown in Fig. 17, and the total reflection calculated coefficients were found to be 8.36, 8.61 and 8.13% respectively.

Each of the unusual spectra have peak frequencies of between 0.45 Hz and 0.5 Hz, around 2–3% steepness, and large spreading. Despite having vastly different spectral forms they have near identical reflection coefficients, consistent with the results shown in Fig. 12. This supports previous findings that peak frequency and steepness are the main parameters to which absorption effectiveness is sensitive to, along with some sensitivity to directional spreading.

## 4. Discussion

### 4.1. Method limitations and sensitivity

#### 4.1.1. Effect of in-line reflection level

The presence of in-line reflections alter the phases and phase differences measured at the gauges, and hence causes an apparent angle estimation error through Eq. (3). The effect of this can be understood by looking at the resulting Fourier coefficients in the presence of such reflections.

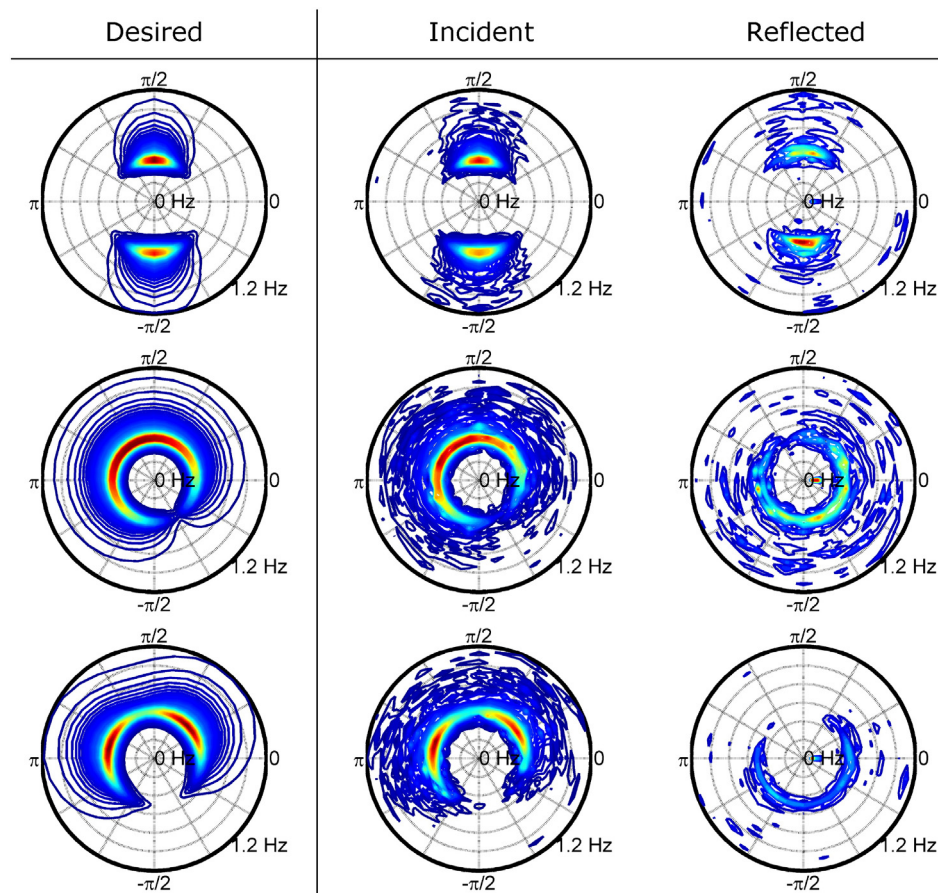


**Fig. 17.** Incident and reflected directional spectrum outputs for complex spectra defined in Table 3. Energy density [ $\text{m}^2/\text{s}/\text{rad}$ ] is shown by the colour, relative to the peak of each spectrum. (For interpretation of the references to colour in this figure legend, the reader is referred to the web version of this article.)

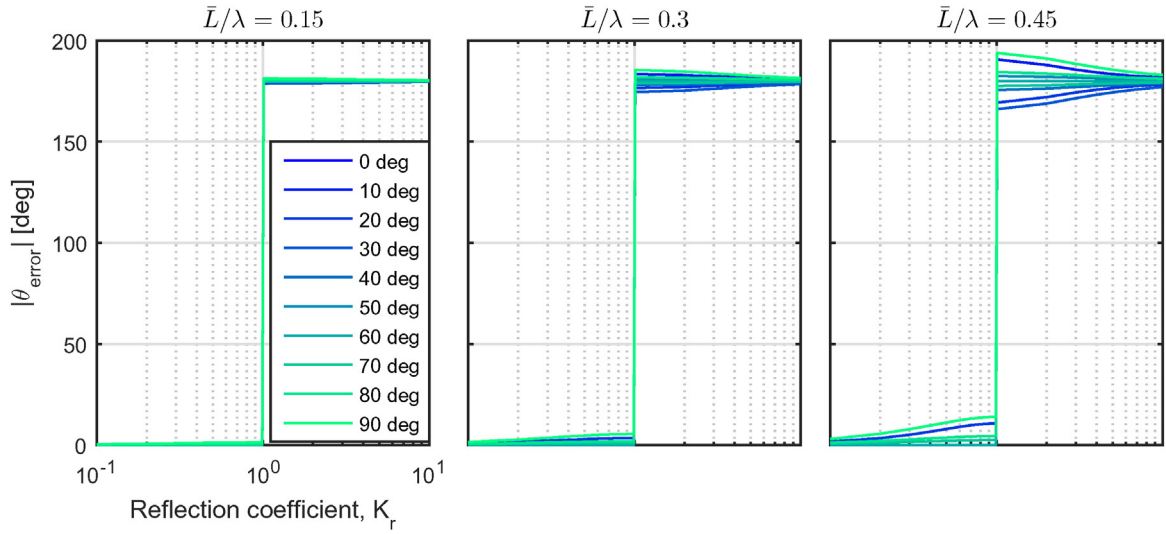


Fig. 18. Effect of in-line reflection coefficient, wave angle and relative separation magnitude on apparent angle calculation.

Surface elevations in the presence of in-line reflections, at  $[x,y]$ , can be modelled as:

$$\begin{aligned} \eta(x,y,t) = & \sum_{n=1}^N A_{inc,i} \cos(k_i(x \cos\alpha_{inc,i} + y \sin\alpha_{inc,i}) + \Phi_{inc,i} + \omega_i t) \\ & + K_{r,i} A_{inc,i} \cos(-k_i(x \cos\alpha_{inc,i} + y \sin\alpha_{inc,i}) \\ & + \Phi_{inc,i} + \Phi_{ref,i} + \omega_i t). \end{aligned} \quad (20)$$

Defining  $k_{i,xy} = k_i(x_n \cos\alpha_{inc,i} + y_n \sin\alpha_{inc,i})$ , and  $k_{r,i} = K_{r,i} e^{i\Phi_{ref,i}}$ , the resulting Fourier coefficients at gauge n can be expressed as:

$$\begin{aligned} a_{i,n} = & a_{inc,i} e^{ik_{i,xy}} + a_{inc,i} k_{r,i} e^{-ik_{i,xy}} \\ = & a_{inc,i} [\cos(k_{i,xy}) + i \sin(k_{i,xy})] + a_{inc,i} k_{r,i} [\cos(k_{i,xy}) - i \sin(k_{i,xy})] \\ = & a_{inc,i} (1 - k_{r,i}) i \sin(k_{i,xy}) + a_{inc,i} (1 + k_{r,i}) \cos(k_{i,xy}). \end{aligned} \quad (21)$$

The expected phase at gauge n is therefore:

$$\Phi_{n,i} = a \tan \left[ \frac{\tan(k_{i,xy})(1 - k_{r,i})}{(1 + k_{r,i})} \right]. \quad (22)$$

Apparent angle for each gauge triad is calculated using:

$$\alpha_{apparent,i} = \tan^{-1} \left[ \frac{(x_1 - x_2)\Phi_{i,13} - (x_1 - x_3)\Phi_{i,12}}{(y_1 - y_3)\Phi_{i,12} - (y_1 - y_2)\Phi_{i,13}} / \text{sgn}(P) \right] \quad (23)$$

where:

$$\Phi_{i,mn} = \Phi_{m,i} - \Phi_{n,i}. \quad (24)$$

From Eq. (22) it can be seen that phases and phase differences at the gauge locations are heavily influenced by the magnitude of the reflection coefficient,  $K_{r,i}$ . However the extent with which this alters the resulting angle estimation depends on the relative change in  $\Phi_{i,13}$  to  $\Phi_{i,12}$ , which is a function of the angle relative to the triad orientation, along with the magnitude of the separations relative to the wavelength.

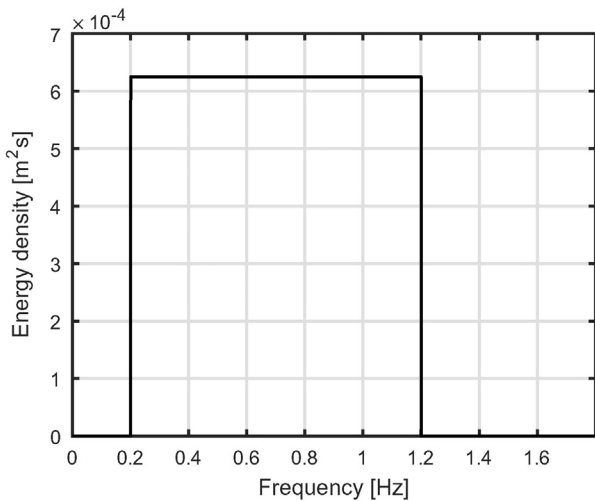


Fig. 19. Uni-directional spectrum for numerical sensitivity analysis.  $H_{m0} = 0.2$ . For the simulations, an incident angle of  $\theta = 22.5^\circ$  has been used.

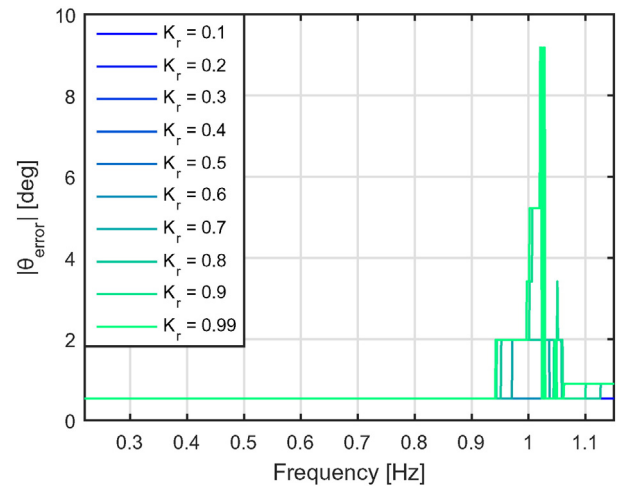


Fig. 20. Angle error for broad-banded spectrum shown in Fig. 19 for various levels of in-line reflection.



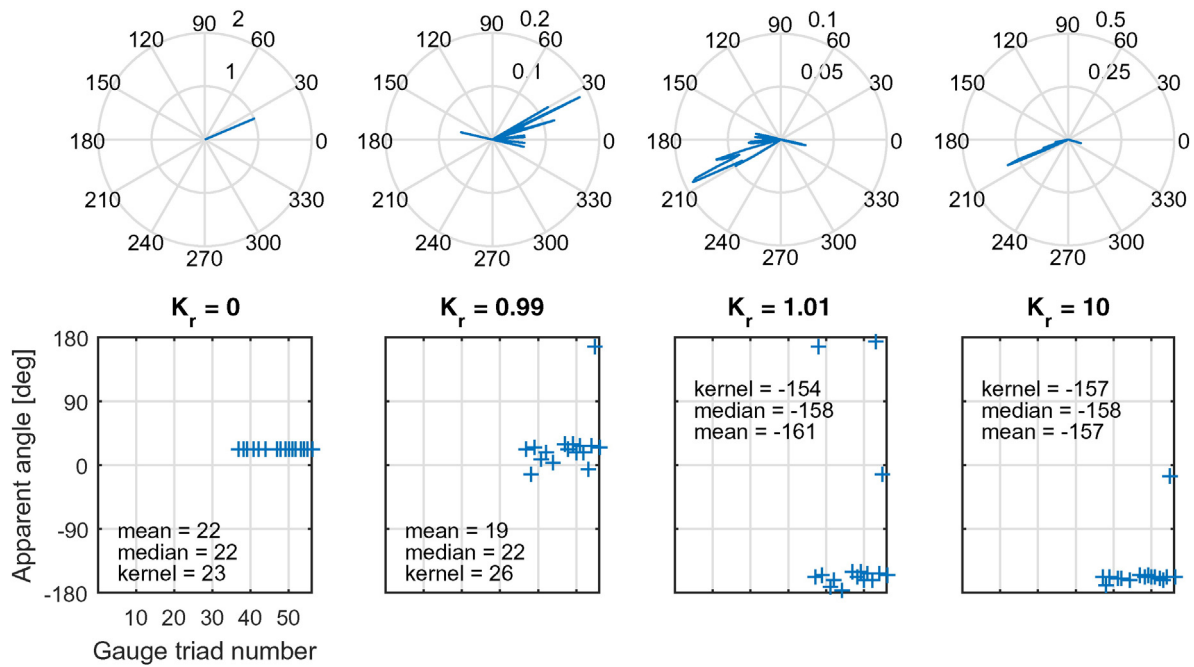


Fig. 21. Individual angle estimates for 1 Hz components of spectrum shown in Fig. 19. Shown with in-line reflection levels of 0, 0.99, 1.01 and 10, along with the resulting kernel density estimates.

Fig. 18 shows the expected angular error for a single equilateral gauge triad as a function of the reflection coefficient, incident angle and relative separation magnitude.  $K_r$  values between 0 to 10 have been used to assess whether the PTPD method presented identifies the ‘reflected’ component as the incident direction if  $K_r > 1$ . From Fig. 18 it is apparent that the method does find the correct ‘dominant’ angle when  $K_r > 1$ .

It is clear that if gauge separations are small then the angle calculation is relatively unaffected by the level of reflection. Practically, however, if gauge separations are too small relative to all frequency components, position error and noise will alter the measured phases more greatly and hence cause increased errors in the apparent angle estimates.

As expected, when reflection levels are low the angular estimates are also largely unaffected. When reflections are large, however, the incident angle relative to the gauge triad orientation becomes important, highly influencing the values of individual angle estimates. Overall the effect of these poor individual estimates can be minimised by designing a wave gauge array so that for each frequency (wavelength) there is a uniform co-array distribution of valid separations. If this is the case, using all of the estimates, the kernel density estimate approach discussed in Section 2.3.1 should be able to provide the correct incident angle.

To assess how the kernel density approach with the array layout shown in Fig. 3 deals with different levels of reflection, a numerical simulation has been carried out, using a uni-directional broad-banded spectrum with frequency independent in-line reflections. This spectrum has been used as it covers the operational frequency range of the tank (0.2 → 1.2 Hz), whilst enabling easy analysis and viewing of results. This spectrum is shown in Fig. 19 and is also used for the sensitivity analysis shown in Section 4.1.2.

Fig. 20 shows the angular error resulting from the simulation. It is clear that the combination of the array and method used performs very well for frequencies up to 0.95 Hz, regardless of the level of reflection. The error shown is purely a function of the number of bins used for the kernel density estimate (250). When reflection is relatively low ( $K_r < 0.5$ ) there is also no perceived error in the angle estimate, at any frequency. This shows that the array-method combination performs very well in general, especially for the level of reflection present in the (empty) FloWave basin. Once this initial angle is effectively identified

the subsequent in-line reflection analysis will then be correct, which can be seen in Fig. 23 when the oblique reflection angle is 0°.

Errors arise from 0.95 Hz onwards when the reflection coefficient is over 0.5, due to the smaller number of valid gauge triads (see Fig. 6). This means that poor individual estimates have a greater effect on the final angle calculation, a result of the combined effect of larger reflections, triad orientation and large relative separations. Individual estimates for 1 Hz with a range of reflection scenarios are illustrated in Fig. 21, demonstrating how individual estimates are affected by reflection levels and how the kernel density estimate mitigates the effect of these on the final angle values.

Where large reflections and high wave frequencies are present it may be necessary to use an array with additional gauges placed closer together. This would ensure that there are enough gauge triads with

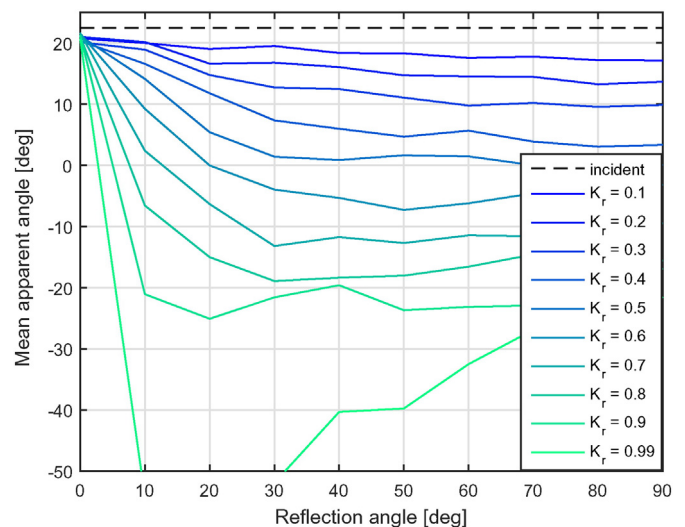


Fig. 22. Effect of reflection level and angle on the mean apparent angle (over all frequencies).

separations less than  $0.45\lambda_i$ , thus improving the high frequency estimates. For the levels of reflection present in the empty tank the current array layout should be suitable for identifying the correct incident angle regardless of frequency. That is, under the assumption that position error and noise are negligible, and more importantly, that reflections can be assumed to be in-line. This will be discussed in Section 4.1.2.

4.1.2. Effect of reflection angle and curvature

4.1.2.1. Oblique reflections. In Section 4.1.1 it was found that the level of in-line reflection does not greatly affect the correct identification of the incident angle when using the current implementation of the method in combination with the wave gauge array. This additionally enables a correct in-line reflection analysis to take place. If, however, the reflections are not in-line then this is no longer the case.

Introducing a change in reflected angle,  $\Delta\alpha_{ref,i}$ , the surface elevations become:

$$\eta(x, y, t) = \sum_{n=1}^N A_{inc,i} \cos(k_i(x \cos\alpha_{inc,i} + y \sin\alpha_{inc,i}) + \Phi_{inc,i} + w_i t) + K_{r,i} A_{inc,i} \cos(-k_i(x \cos(\alpha_{inc,i} + \Delta\alpha_{ref,i}) + y \sin(\alpha_{inc,i} + \Delta\alpha_{ref,i})) + \Phi_{inc,i} + \Phi_{ref,i} + w_i t). \tag{25}$$

Defining  $k_{i,\alpha,xy} = k_i(x \cos(\alpha_{inc,i} + \Delta\alpha_{ref,i}) + y \sin(\alpha_{inc,i} + \Delta\alpha_{ref,i}))$ , the resulting phases can be shown to be:

$$\Phi_{n,i} = a \tan \left[ \frac{a_{inc,i} \sin(k_{i,xy}) - k_{r,i} a_{inc,i} \sin(k_{i,\alpha,xy})}{a_{inc,i} \cos(k_{i,xy}) + k_{r,i} a_{inc,i} \cos(k_{i,\alpha,xy})} \right]. \tag{26}$$

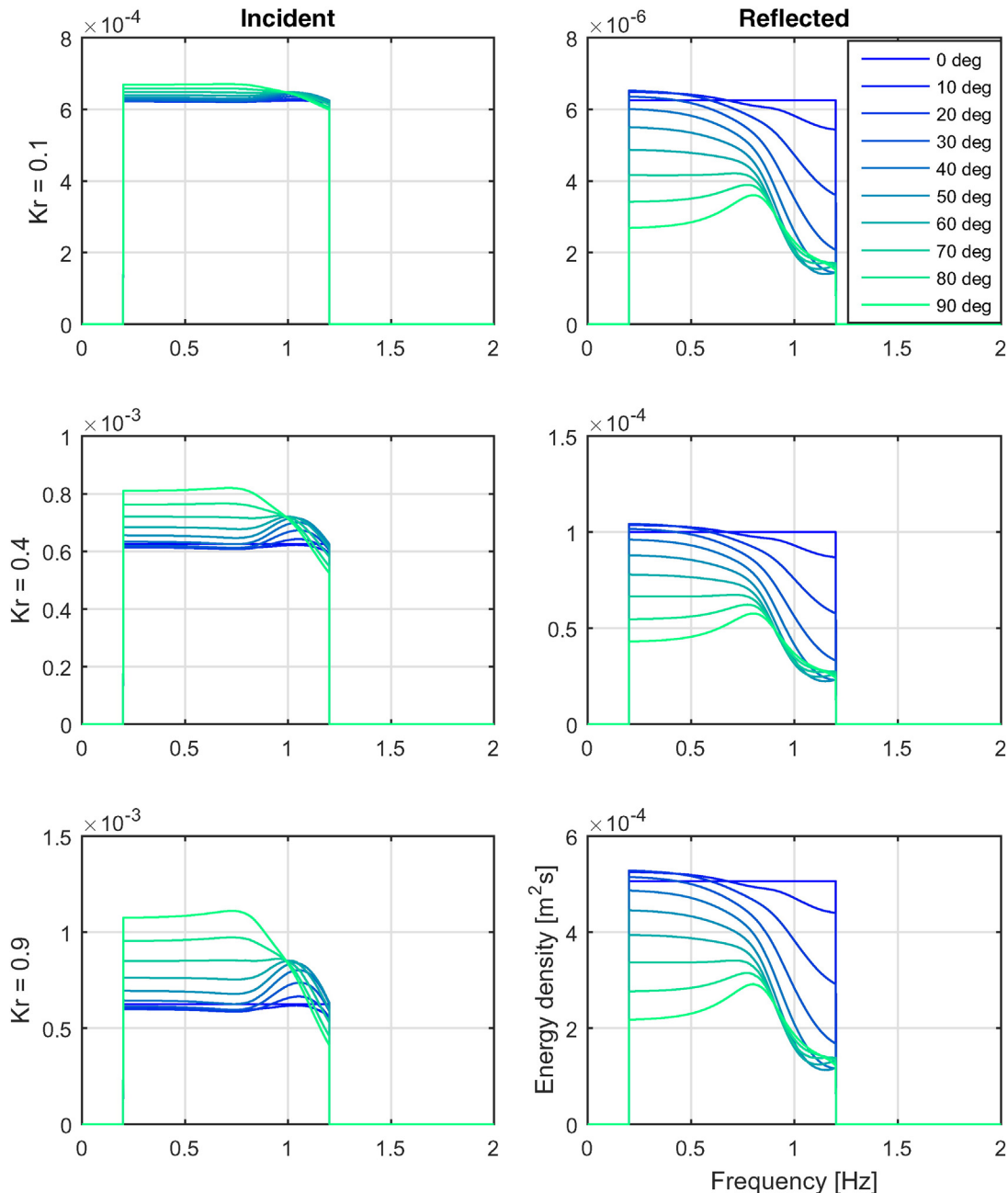


Fig. 23. Effect of reflection level and angle on the separation of incident and reflected spectra.

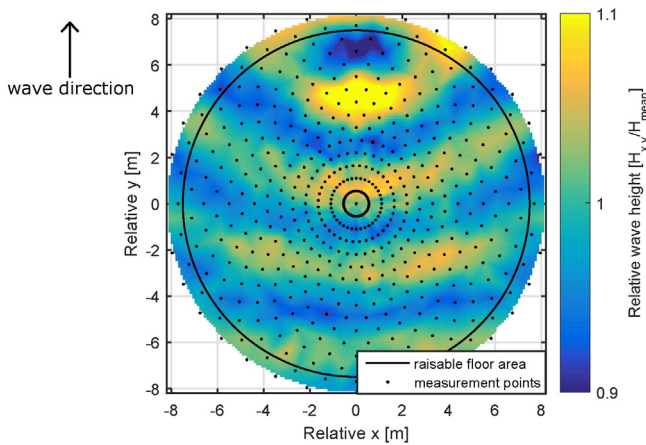


Fig. 24. Spatial map of wave height variation for 0.45 Hz regular waves (2% steepness). Shows reflected wave curvature over the tank operational area (roughly equal to floor area).

It can be seen from Eq. (26) that the phase differences will be altered by the magnitude of  $\Delta\alpha_{ref,i}$  in addition to the level of reflection and array layout. The difference here compared with the in-line reflection analysis, Eq. (22), is that when the angles are calculated using Eq. (3), the ‘direction’ of the angular error is now no longer solely a function of the triad layout, and as such does not ‘average’ out over multiple estimates. All angle estimates now contain a consistent error as a function of  $\Delta\alpha_{ref,i}$ .

Using the spectrum shown in Fig. 19, and simulating the oblique reflections over the array we can observe this consistent shift in angle estimate, shown in Fig. 22. This shows that if there are sizeable reflections with even a small reflection angle then the PTPD approach cannot be used to effectively identify the incident angle.

As discussed in Section 4.2.2 it is not always necessary to estimate the incident angle. To further assess how oblique reflections affect the isolation of incident and reflected spectra the incident angles are assumed to be known. Fig. 23 shows how the level, and angle of reflection, affect the isolation of incident and reflected spectra. As expected, this shows that it is not appropriate to use in-line reflection analysis when the reflections are oblique relative to the incident. This is because the phase differences are no longer a function of the ‘in-line’ gauge separations assumed in the analysis. It may however be suggested that results are still somewhat useful if the reflection angle is low, perhaps less than 20°.

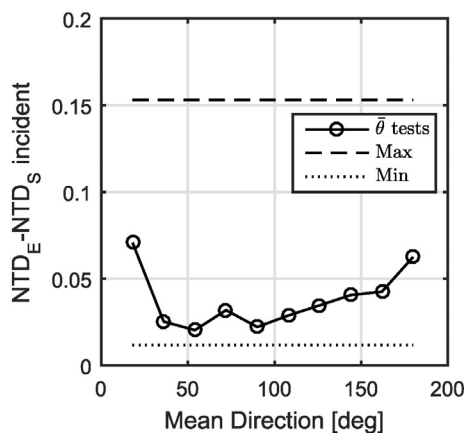


Fig. 25. Effect of mean direction on perceived sea state performance. Maximum and minimum values of the test programme shown in dashed lines.

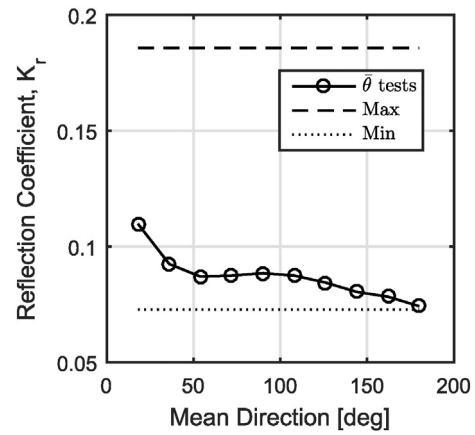


Fig. 26. Effect of mean direction on perceived reflection coefficient. Maximum and minimum values of the test programme shown in dashed lines.

4.1.2.2. *Curved reflections.* When reflections are curved or directionally spread, there will be larger variation in the individual angle estimates generated using the gauge triad combinations. If the mean direction of the curved waves is not opposite the incident, then similar behaviour is to be expected to the oblique wave analysis, but with additional scatter. If, however the mean direction of the curved waves opposes the incident, then the correct incident angle can be identified with an appropriate array, and a meaningful representative in-line reflection analysis procedure can take place. This is the case at FloWave.

The circular wave basin at FloWave ensures that the mean direction of reflected components opposes the incident direction. The circular shape also means that the reflected components are curved, as a function of the wave basin geometry and the angular dependency of the tank transfer function.

Reflected wave curvature has been analysed through the spatial variation of measured wave heights. As it is known that the incident waves are long crested and uniform, the variation in wave height is solely a function of the curved reflected components interacting with the incident waves. An example ‘spatial map’ is shown in Fig. 24 for 0.45 Hz regular waves, noting that from further tests the curvature of these reflections appears to be independent of wave frequency. Over the small array area (1 m<sup>2</sup>) the assumption that curvature is negligible for the purpose of reflection analysis seems appropriate.

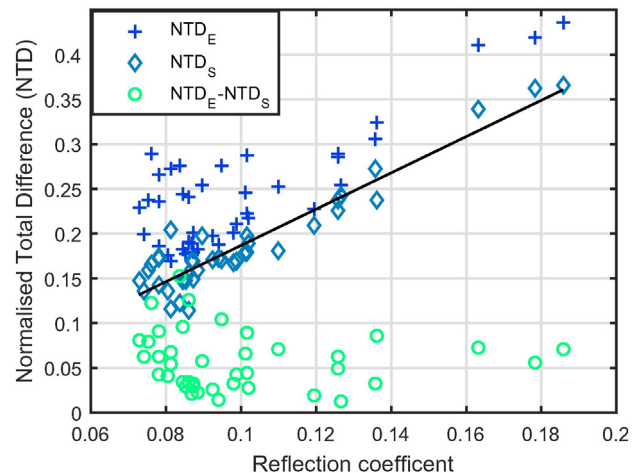


Fig. 27. Normalised total difference for incident spectra as a function of reflection coefficient. Linear fit overlaid for  $NTD_S$  v  $K_r$ , with an  $r^2$  value of 0.89.



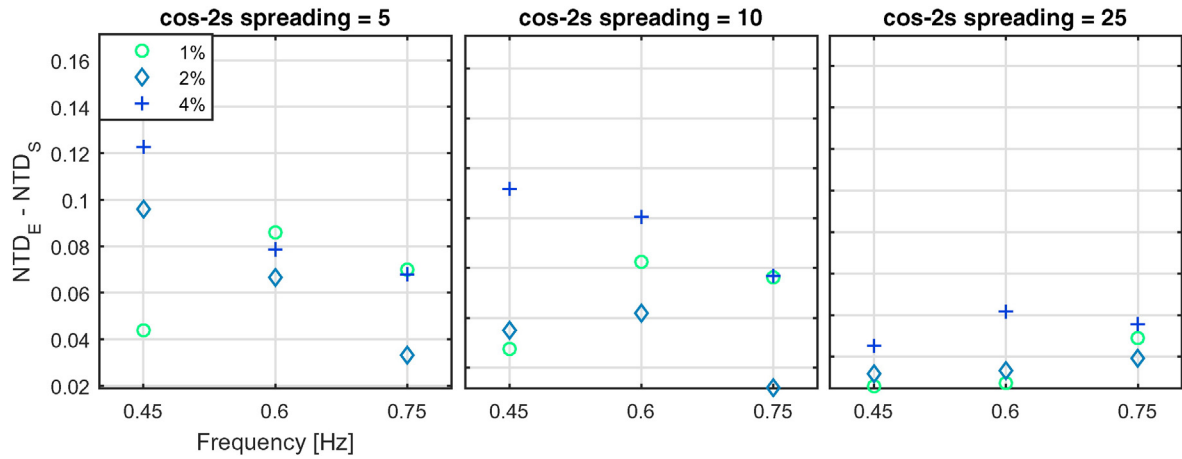


Fig. 28. Directional distribution error as a function of spreading, steepness and peak frequency.

The results presented here clearly shows that for the level of reflection and curvature present, the incident angle can be effectively identified using PTPD approach with the wave gauge array shown in Fig. 3. Once these are identified the co-array uniformity and least squares approach of the reflection analysis should ensure that the representative in-line reflection coefficients are valid despite these small levels of curvature. This should give a very good estimate of the incident and reflected spectra, and time-series, over the array area. This approach means that sea states can be effectively characterised in a particular location (generally in the tank centre), prior to use in a test programme with a model installed.

From Fig. 24, it is apparent that the effective reflection coefficient is not constant, and in fact varies in the in-line direction due to circular focussing effects. As a result of this, and the reflected wave curvature, it is clear that the reflected directional spectrum is spatially variable. This means that although the isolation of incident and reflected spectra, and time-series over the array area gives reliable results, using this 2D approach to extrapolate far from the measurement area will not be accurate. However, through knowledge of the wave curvature and in-line dependency of the reflection coefficient, it should be possible to alter the energy density and angles in the reflected spectrum, and amplitudes and phases in the time-series reconstructions to provide reasonable estimates over the tank area, if desired.

4.1.3. Influence of mean direction

The wave generating capability at FloWave is designed to be directionally independent, meaning that any change in mean wave propagation direction should not influence the sea state performance. Any perceived changes should therefore be attributed to the array layout, and the method itself.

Figs. 25 and 26 show the perceived reflection coefficient and directional NTD variation incurred by varying mean direction for a single sea state. The sea state used is detailed in Table 2. It can be seen in Fig. 26 that when altering the mean direction, the perceived reflections

also vary. This is coupled with variation in the perceived directional distribution error.

Without the presence of reflections, noise, or position error, there would be no error in the measured propagation directions, and hence no discrepancy in the directional distribution. Of these factors, the presence of reflections is probably the largest contributor in most circumstances. It is observed to have a consistent effect on both the relative phases, and the amplitudes at the gauge locations.

As the mean direction changes, the array layout plays an important role, as the relative reflection and error-influenced phase differences are dependent on the projected in-line separations. These deviations cause differences in the perceived angles and hence incur a varied and largely unpredictable directional distribution error. A portion of the perceived directional deviation for any sea state is therefore a complex function of the induced phase errors (mostly reflection based), and the array layout.

4.1.4. Influence of primary sea state parameters on performance

Analysing the variation in NTD, it is difficult to assess what proportion of this difference is the result of actual sea state deviation, and what can be attributed to the array-methodology effectiveness under various conditions. This was one of the reasons for using  $NTD_E - NTD_S$

Table 5  
Number of gauge combinations available.

Number of gauges	Number of combinations
3	56
4	70
5	56
6	28
7	8
8	1

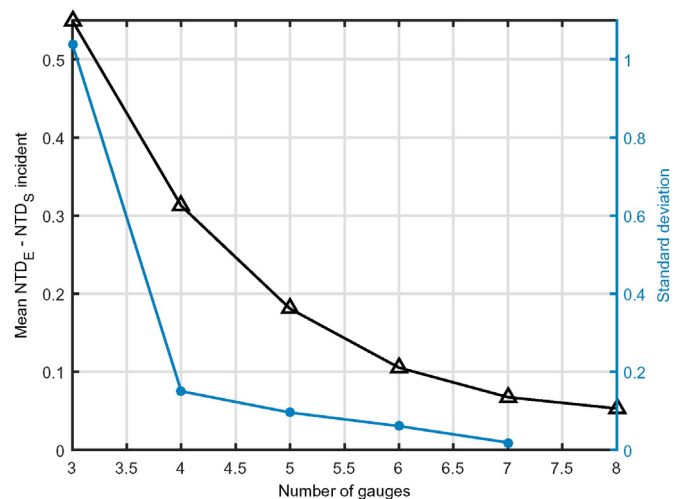


Fig. 29. Influence the number of gauges has on the directional distribution error, along with the standard deviation of this error.

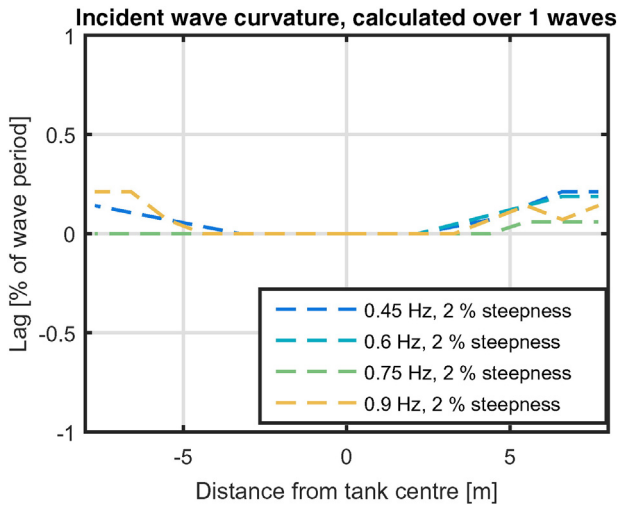


Fig. 30. Phase lag between wave gauges in a line perpendicular to the expected wave propagation direction. Shows that the waves are produced at the correct angle and have negligible curvature.

in Section 3.5.1, removing the frequency spectrum deviation, and focusing on the directional distribution reconstruction.

The total deviation,  $NTD_E$ , and the frequency spectrum deviation,  $NTD_S$ , essentially show the same dependencies as the reflection coefficient, shown in Fig. 12. It appears that higher peak frequency sea states with low steepness incur both greater reflections, and larger deviations in the incident spectrum simultaneously. The correlation between  $NTD$  and reflection coefficient can be seen in Fig. 27.

The directional deviation metric,  $NTD_E-NTD_S$ , appears not to have a predictable correlation to reflection coefficient, as discussed in Section 4.1.3. Fig. 28 shows the relationship between the directional distribution component, and the primary sea state parameters. The only apparent relationship appears to be a reduced  $NTD$  when spreading is lower ( $s$  is higher). This is potentially expected as the only two parameters affecting directionality are spreading and mean direction, of which, mean direction has been fixed for the main  $3 \times 3 \times 3$  test matrix.

4.1.5. Influence of number of gauges

As discussed in Section 4.1.3 increasing the number of gauges, if positioned correctly, should reduce the sensitivity to wave directionality. In general, additional gauges should give rise to improved estimates

and reduced directional discrepancy between target and measured spectra. To explore the effect of the number of gauges all gauge combinations with 3 or more gauges have been assessed under an individual sea state (Table 2,  $\bar{\theta} = 36^\circ$ ). The number of combinations for a desired number of gauges is shown in Table 5, whilst the mean directional deviation and the standard deviation of this between array layouts is shown in Fig. 29. As expected, the mean directional deviation reduces with the use of more gauges. The standard deviation of the directional deviation is also shown, describing the expected variation in performance when using different sets of gauges.

Increasing the number of gauges will further reduce both the directional deviation and the variation between hypothetical gauge subsets. As the gauge combination choice is analogous to an effective change in wave direction, this will further reduce the sensitivity of an array to direction, thus improving the reliability of the estimates under a variety of wave conditions.

4.2. Alternative applications

4.2.1. No reflection analysis: PTPD approach only

As demonstrated in Draycott et al. (2015), using the PTPD approach to reconstruct directional spectra at FloWave works effectively without the addition of reflection analysis. This works particularly well at the FloWave facility (or other circular wave basins with active absorption) as the reflections are low, and can be approximated as in-line. It should also be effective for tanks with different geometry, providing reflections are relatively low, and the reflection angle isn't very large (see Fig. 22). If this is the case then the incident directions should be effectively identified, and a more accurate representation of the incident directional spectrum should be attained than when using the EMEP or BDM approaches.

4.2.2. No angle calculation: assumed incident angles

Sections 4.1.1 and 4.1.2 show that under certain conditions the presence of reflections can introduce errors in the incident angle calculation. This, consequently, means that the projected in-line reflection analysis is done at a slightly incorrect angle thus meaning that the reflection coefficients themselves will be incorrectly calculated, along with the incident and reflected spectra. If it can be assumed that the incident wave propagation angles are known, and precisely produced, then reflection coefficients can be calculated more accurately, whilst giving a better representation of the reflected wave field.

Fig. 30 shows the relative time lag between gauges mounted perpendicular to the expected wave propagation direction, for a variety of regular waves with different frequencies. Sampled at 128 Hz, it can be seen that the phase lags are all less than 1 time step. This shows that the

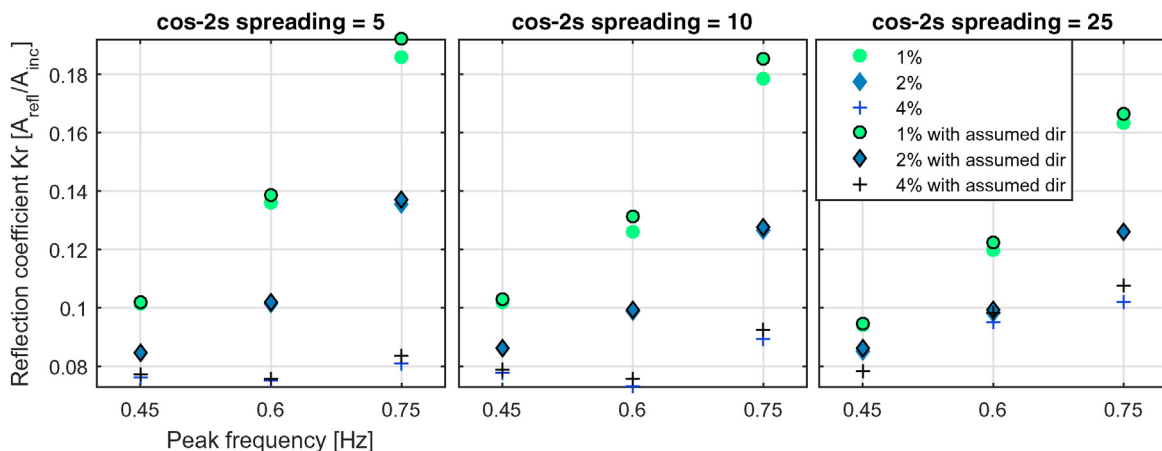


Fig. 31. Influence assuming the incident direction has on the reflection coefficient calculation.

desired angle is precisely produced with negligible curvature, at least from  $\pm 8$  m from the tank centre. This analysis was done on only the first few regular waves (to avoid reflections), however it is probably a good assumption that the generation capability is not greatly affected by either simultaneous absorption or the generation of multi-directional sea states. Therefore the incident angles can be assumed correct at FloWave.

The resulting overall reflection coefficients when the assumed input angles are used are shown in Fig. 31. It is apparent that when the reflections are larger, the greater the error in the computed reflection coefficient, highlighting this ‘feedback loop’ problem. In general however, the reflection coefficients agree very well and it is clear that the computations where angle isn’t assumed will provide adequate practical reflection estimations in the majority of cases.

#### 4.3. Further work

Further work aims to include an extension to handle oblique reflections, potentially using a procedure similar to Wang et al. (2008). This extension, along with an understanding of the geometry in question would enable directional reflections to be calculated accurately for other objects such as rectangular tanks, or indeed other structures and devices. The idea of enabling of reflections to be resolved using double summation approaches, or as curved components will also be explored, enabling the reflected components to have a spread at each frequency.

### 5. Conclusions

The directional characteristics of sea states are often relevant to ocean and coastal engineering problems. The capability of wave basins to produce more complex multidirectional sea states has expanded in recent years, with many facilities now having wavemakers along multiple boundaries, or in the case of circular tanks, around the entire circumference. The ability to generate more complex spectra, including those with extreme spreading and multi-modality, brings about challenges in validating and calibrating these sea states and highlights the limitations in the established measurement techniques. To this end the SPAIR method has been developed. A single-summation method of wave generation has been used to generate a range of directional sea state conditions in a circular wave tank, FloWave. A phase-time-path difference approach has then been used to calculate wave propagation angles, before frequency-dependent in-line reflection analysis is performed.

This method, SPAIR, has proved to be highly effective in the measurement of multidirectional sea states within a circular wave tank, providing both incident and reflected directional spectra, and reconstructed time-series. The method has been demonstrated with both standard parametric and more complex multi-modal and extremely spread seas. When this single-summation method of wave generation is used, the PTPD-based reconstruction method has shown to be more effective at validating directional sea states

than either the EMEP or BDM approaches, reducing the mean apparent directional deviation from 16.1% (EMEP), and 21.7% (BDM), down to 5.93%.

Sensitivity analysis shows that method itself, in combination with the wave gauge array, has very low sensitivity the level of in-line reflection, particularly for the range expected at the FloWave facility. However, high sensitivity is displayed to the presence of oblique reflections, something which future work aims to deal with.

### Acknowledgements

The authors would like to thank the Energy Technology Institute and the Research Council UK Energy Programme for funding this research as part of the IDCORE programme (EP/J500847/1). In addition we would like to thank the UK Engineering and Physical Science Research Council for funding towards the creation of the FloWave Ocean Energy Research Facility (EP/I02932X/1).

### References

- Benoit, M.P., Frigaard, P., Schaffer, H.A., 1997. Analysing multidirectional wave spectra: a tentative classification of available methods. Assoc. Hydraulic Res. Seminar: Multidirectional Waves.
- Draycott, S., Davey, T., Ingram, D.M., Lawrence, J., Day, A., Johanning, L., 2015. Using a Phase-Time-Path-Difference Approach to measure directional wave spectra in FloWave. EWTEC Conference Proceedings.
- Esteva, D., 1976. Wave direction computations with three gage arrays. Coastal Engineering Proceedings.
- Fernandes, A.A., Sarma, Y.V.B., Menon, H.B., 2000. Directional spectrum of ocean waves from array measurements using phase/time/path difference methods. Ocean Eng. 27 (4), 345–363.
- Goda, Y., Suzuki, T., 1976. Estimation of incident and reflected waves in random wave experiments. Coastal Engineering Proceedings, pp. 828–845.
- Gyongy, I., Bruce, T., Bryden, I., 2014. Numerical analysis of force-feedback control in a circular tank. Appl. Ocean Res. 47, 329–343 (August).
- Hashimoto, N., Konbune, K., 1988. Directional spectrum estimation from a Bayesian approach. Coastal Engineering Proceedings, pp. 62–76.
- Hashimoto, N., Nagai, T., Asai, T., 1994. Extension of the maximum entropy principle method for directional wave spectrum estimation. Coastal Engineering Proceedings, pp. 232–246.
- Haubrich, R.A., 1968. Array Des. 58 (3), 977–991.
- Ingram, D., Wallace, R., Robinson, A., Bryden, I., 2014. The design and commissioning of the first, circular, combined current and wave test basin. Flow3d.com.
- Krogstad, H.E., 1988. Maximum likelihood estimation of ocean wave spectra from general arrays of wave gauges. Modeling, Identification and Control.
- Mandel, L., Wolf, E., 1976. Spectral coherence and the concept of cross-spectral purity. J. Opt. Soc. Am. 66 (6), 529.
- Mansard, E.P.D., Funke, E.R., 1980. The measurement of incident and reflected spectra using a least squares method. Coastal Engineering Proceedings, pp. 154–172.
- Miles, M.D., Funke, E.R., 1989. A Comparison of Methods for Synthesis of Directional Seas.
- Pascal, R.C.R., 2012. Quantification of the Influence of Directional Sea State Parameters Over the Performances of Wave Energy Converters.
- Wang, S.K., Hsu, T.W., Weng, W.K., Ou, S.H., 2008. A three-point method for estimating wave reflection of obliquely incident waves over a sloping bottom. Coast. Eng. 55 (2), 125–138 (February).
- Zelt, J.A., Skjelbreia, J., 1992. Estimating incident and reflected wave fields using an arbitrary number of wave gauges. Coast. Eng. Proc. 1, 777–789.